Simulation of interaction between wind farm and power system

Sørensen, Poul Ejnar; Hansen, Anca Daniela; Janosi, L.; Bech, J.; Bak-Jensen, B.

Publication date:
2002

Document Version
Publisher's PDF, also known as Version of record

Risø-R-1281(EN)

Simulation of Interaction between Wind Farm and Power System

Poul Sørensen, Anca Hansen, Lorand Janosi, John Bech and Birgitte Bak-Jensen

Risø National Laboratory, Roskilde
December 2001

Abstract A dynamic model of the wind farm Hagesholm has been implemented in the dedicated power system simulation program DIgSILENT. The wind farm consists of six 2MW NM2000/72 wind turbines from NEG-Micon. The model has been verified using simultaneous power quality measurements on the 10 kV terminals of a single wind turbine and power performance measurements on two wind turbines. The verification shows a generally good agreement between simulations and measurements, although the simulations at higher wind speeds seem to underestimate the power and voltage fluctuations. A way to improve the simulation at higher wind speeds is suggested.

This report has passed the internal review performed by

Peter Hauge Madsen

Frede Blaabjerg

ISBN 87-550-2912-4
ISBN 87-550-2913-2 (Internet)
ISSN 0106-2840

Print: Pitney Bowes Management Services Denmark A/S, 2001

Contents

Preface

This report describes the results of the project titled “Simulation of wind power plants”. The project was carried out in a cooperation between Risø National Laboratory, Aalborg University and DanControl Engineering A/S, funded by the Danish Energy Agency contract number 1363/00-0003. Besides, North-west Sealand Energy Supply Company, NVE, has contributed to the work with own funding.

1 Introduction

The present report describes the results of a project titled “Simulation of wind power plants”. The title of the project reflects the need to look at large wind farms as power plants, as a result of the increased penetration of wind energy in the power systems many places in the world. To obtain an optimal integration of high penetration of wind energy in the system, the wind large wind farms must be able to replace other power plants, i.e. be able to participate in the control and stabilisation of the power system. If e.g. a large wind farm trips due to a grid fault, the power system will suffer from a severe loss of supply.

The main result of the project is a verified model of a wind farm, which can be used to study and improve the power plant characteristics of the wind farm, and a tentative assessment of the power quality of the wind farm, based on simulations with the developed model and verified by measurements.

The installation of wind turbines in power systems has developed rapidly through the last 20 years. The national and international growth rates and policies indicate that this development will continue. During 1999, 3920 MW wind turbine capacity was installed in the world, making up a total accumulated installation of 13932 MW wind power in the end of 1999 [1].

In Denmark, the accumulated installed wind turbine capacity was 2340 MW in the end of 2000, and today approximately 15 % of the electricity consumed in Denmark is generated from wind power. Moreover, in the official Danish energy strategy Energy 21 [2], the target is to reach 50 % of electricity consumption from wind power in 2030. This target is based on offshore, with 4000 MW wind turbines installed in 5 dedicated offshore areas in Denmark.

Such a development will influence significantly the operation of the power systems in Denmark. Even though the western part of Denmark is AC connected to the strong Central European power system, and the eastern part is AC connected to the Nordic power system, this wind energy development will influence the control, power quality and voltage stability issues of the power system. Therefore, the future wind farms will need power plant properties, which enables the wind farms to operate more like conventional power plants.

An example of the need to provide wind farms with power plant properties is the practice for wind turbine control in the event of grid abnormalities, e.g. due to grid faults. The practice so far has been to disconnect wind turbines from the grid when a grid abnormality is detected by the wind turbine control system. This strategy has served as a protection of the wind turbines as well as the grid. However, with the very large wind farms planned for the future, this control strategy will not be sufficient any more, because it can lead to sudden loss of power, which can cause problem to the control of the power system.

The increased wind energy development is also reflected in the requirements for grid connection of wind turbines. National standards for power quality of wind turbines have been supplemented by a new IEC 61400-21 standard for measurement and assessment of power quality of grid connected wind turbines [3]. The methods described in IEC61400-21 are already applied in many national requirements for grid connection of wind turbines to the distribution system, e.g. the Danish Utilities Research Institute, DEFUs KR-111 [4] in Denmark.

Because of the planned offshore development in Denmark, the Danish transmission system operators Eltra and Elkraft System have issued specific requirements for connection of large wind farms to the transmission system, [5] and [6]. Besides power quality issues, these requirements also deal with the

control of the wind farms and the interaction between the wind farm and the power system in the event of a grid fault.

These standards and requirements all reflect the need to assess the interaction between the wind farms and the power systems. However, standards and requirements often use simplifications of complex technical issues, which often need more advanced methods to be assessed. Power system simulation with reliable models for wind farms can provide the technical basis for such assessments.

In the requirements of the Danish transmission system operators, it is explicitly stated that the wind farm owner is responsible to provide the required simulation models to demonstrate the interaction between the wind farm and the power system in the event of grid faults. Such a requirement makes it even more necessary to provide and verify reliable models for the dynamic interaction between the wind farms and the power system.

According to the requirements of the Danish transmission system operators, models for simulation of the behaviour in the event of grid faults are needed to verify the interaction between the power system and the wind farm in these cases. For this purpose, electromagnetic transient models of the electric components are required, together with models for the mechanical and aerodynamic behaviour of the wind turbines.

Detailed assessments of power quality and of control strategies for wind farms also call for dynamic simulation models, which take into account the interaction between the dynamics of the wind turbines and the grid. For power quality and control strategy studies, dynamic wind models are also essential. Although the appropriate detailing of some of the models depends on the issue of the assessment, there are many similarities between the required models for assessment of power quality, control strategies and wind farm behaviour in the event of grid faults.

Computer models of power systems are widely used by power system utilities to study load flow, steady state voltage stability and dynamic behaviour of power systems. The models presented in this report are implemented in the dedicated power system simulation program Power Factory from DIgSILENT. The Power Factory directly supports the selection of detailing of the models, which is appropriate to the current issue, as explained in chapter 2. As a consequence, the models described in this report can be used for assessment of power quality, control strategies and behaviour in the event of grid faults.

The case, which is modelled in this report, is the 12 MW wind farm in Hagesholm. The wind farm consists of six 2MW NEG-Micon wind turbines. Hagesholm is situated in the flat, diked-in land of Lammefjord on Sealand in Denmark. Half of the wind turbines in the wind farm are owned by the North-West Sealand Energy Supply Company, NVE, while the remaining wind turbines are privately owned. Figure 1 shows four of the six wind turbines in the Hagesholm wind farm.

Figure 1. Four of the six wind turbines in Hagesholm wind farm.

The layout of Hagesholm wind farm is shown in Figure 2. The six wind turbines are of the type NM 2000/72, and use active stall regulation of the blade angles to control the power. As it can be seen from the figure, the six wind turbines are distributed in two rows. The distance between the wind turbines in each row is 200 m, corresponding to approximately three rotor diameters, while the distance between the rows is 500 m.

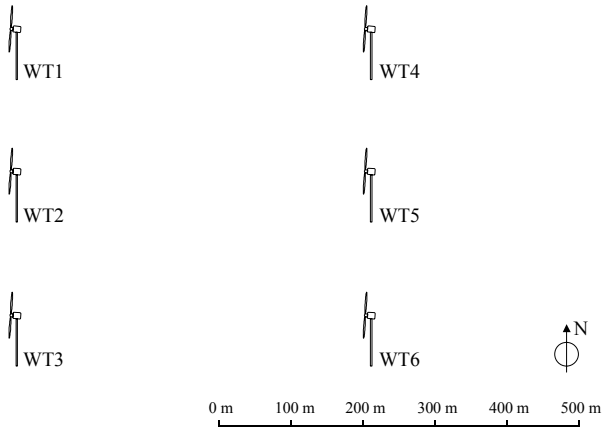

Figure 2. Layout of Hagesholm wind farm.

The model for the Hagesholm wind farm, which is described in this report, has been organised in submodels for the grid, the wind turbines and the wind speeds respectively. These submodels are described in detail in chapter 3, 4 and 5 respectively.

Measurements of power quality on one of the wind turbines in Hagesholm have been performed in the project to verify the model. Moreover, Risø measurements in the Vindeby offshore wind farm and NEG-Micon measurements performed by WINDTEST in Hagesholm have been used. The Vindeby measurements have been used to develop and verify the wind models, based on simultaneous wind speed measurements on two sea masts. The WINDTEST Hagesholm measurements have been used to verify the model predictions of summation of power from two wind turbines, based on simultaneous performance measurements on two wind turbines. The measurement setups and verifications are described in chapters 6 and 7.

To demonstrate the use of the model to assess the interaction between wind farm and grid, the model has been applied to make a tentative assessment of the power quality of the wind farm. This power quality assessment is described in chapter 8.

Finally, the conclusions are summarised in chapter 9. The main conclusion is, that a model for the interaction between wind turbines and grid in a wind farm has been developed and verified, and it has been demonstrated that the model can predict the influence of the wind farm on the power quality.

2 Simulation program

2.1 General

A variety of commercial software packages, dedicated to simulation of power systems, are available on the market. For the present project, Power Factory software from the German company DIgSILENT has been selected, because the Power Factory supports the needs of the project. Other software packages could also support the basic needs of the project, but DIgSILENT combines models with different detailing levels in a very well structured way. Moreover, the industrial partner in the project, DanControl already possessed a license for the Power Factory before the project started.

The Power Factory software provides a simulation environment, which supports two methods for simulations. The first method is based on electromechanical models for the components in the power system, and this method provides RMS values of the simulated variables in the system, i.e. voltages, currents etc. The second method extends the models to include electromagnetic transients, and this method provides instantaneous values of currents and voltages.

Consequently, the detailing of the models for e.g. generators depend on, which type of simulation is selected. This is useful, because the appropriate detailing of the models depends on, which issue the simulations are used to study.

On one hand, for the studies of the behaviour during grid faults, simulations of instantaneous values with detailed models of e.g. generators are required. These simulations consume considerable computer time compared to the period, which is simulated, but only simulations of short periods like a few seconds are required. Therefore, the relatively slow simulation speed is not so important in this case.

On the other hand, simulations of RMS values are more appropriate for most studies of power quality and control issues. One exception from this is harmonics, where instantaneous values are required, as the RMS values simulated with DIgSILENT refer to the fundamental. However, harmonics are not considered for wind turbines without power electronic converters according to IEC 61400-21.

The RMS simulations are much faster than the instantaneous value simulations compared to the period which is simulated. To simulate the influence of the fluctuations in the wind on e.g. flicker emission from the wind farms, long simulation periods are required. According to IEC 61400-21, more than 50 measured ten minutes time series are required to characterise the power quality. These measurements can be replaced by simulations in the early design phase of a wind turbine, or in the design of a wind farm. For a complete power quality

assessment based on simulations, the required extend of simulated time series corresponds to the required extend of measured time series, i.e. more than 50 simulated ten minutes time series.

Another aspect of the simulation program is at which level, the user can use the software. On one hand, it is essential which models are available in the library, because it saves the time to create models if a complete library is available. On the other hand, the user may want to study the exact implementation of the models, and possibly modify the models.

DIgSILENT has a comprehensive library, which is maintained and extended continuously. Together with a graphic interface, this library enables the user to build grid models using a minimum of time. However, the technical documentation of the library models is insufficient. This is a problem, because the implementation of the models is not directly available to the user, which makes it difficult to document and modify the models.

Especially the models for the electric components are inaccessible to the user, and can only be used as black boxes. This is a serious limitation for the use of the program, because one obvious application of the program could be to study e.g. the influence of a new generator concept on the interaction between wind turbines and grid. However, this will only be possible after DIgSILENT has implemented a model for the new generator concept.

For the models of the mechanical and aerodynamic parts of the wind turbines, DIgSILENT provides a graphical environment of composite frames. A composite frame consists of a number of slots, connected by input/output relations. The composite frame and the slots are empty structures, and the slots must be filled with concrete models written in the dynamic simulation language DSL. DIgSILENT provides a comprehensive library of DSL models, and the user can build own models either as modifications of existing models or as completely new models. This feature is essential for modelling of wind turbines and wind speeds, and it has been used extensively in the present project.

2.2 Library models

As mentioned above, DigSilent provides an extensive library of models for electric components in the power system. Many of these models are used in this project as parts of the submodels, and some of them, e.g. transformers and power lines, are used in the grid submodel as well as the wind turbine submodel. As the simulation results strongly depend on these models, the library models for selected components are briefly described below, based on the information from DIgSILENT Power Factory manual [7] and on a note from DIgSILENT on the induction machine models [8].

2.2.1 Induction generator model

The dynamic behaviour of the induction generator plays a significant role for the behaviour of a wind turbine in the event of a grid fault [9]. Also for normal operation as considered for studies of power quality, the induction generator plays an important role.

DIgSILENT provides models for induction generators as well as synchronous generators. The generator models are deeply integrated in the program, and therefore, it will be a very difficult task to implement ones own generator model in the program.

In the present project, the DIgSILENTs library model for induction machines is used to represent the induction generator in the wind turbine. Figure 3 shows the equivalent diagram used by DIgSILENTs induction machine model. It con-

sists of a general model for the stator, which can be combined with three different rotor models, depending on the type of generator.

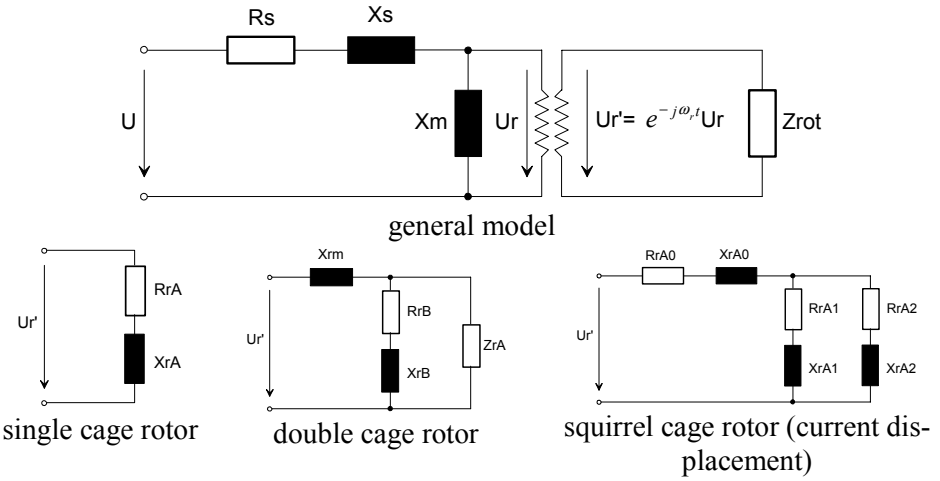

Figure 3. Induction Machine Model in DIgSILENT PowerFactory. Source: Digsilent note on induction machine models [8].

The standard induction machine model is the one shown in Figure 3 for a single cage rotor. This equivalent was also the only one available in the first versions of DIgSILENT. It is sufficient for normal operation, also of generators with squirrel cage. However, for operation outside the linear part of the torque curve, i.e. with high slip, this model is insufficient for machines with squirrel cages. In that case, DIgSILENTs rotor model for squirrel cage provides the rotor current displacement, which is important for operation outside the linear area.

The parameters for the squirrel cage rotor are normally not available directly from data sheets. DIgSILENT helps to overcome this problem by a build in algorithm, which determines the parameters from the measured torque – slip curve, short-circuit test and nameplate values, which are normally available. The parameters can also be entered directly, if they are known, e.g. from tests or simulations with other programs.

2.2.2 Transformer model

The transformer model used in this project is provided by DIgSILENT.

The implementation in DigSilent is presented as follows. The representation of the positive sequence equivalent diagram is shown in the next figure and includes a generalized tap–changer model (phase and magnitude). The tap-changer in the figure has been drawn at the LV side by choice.

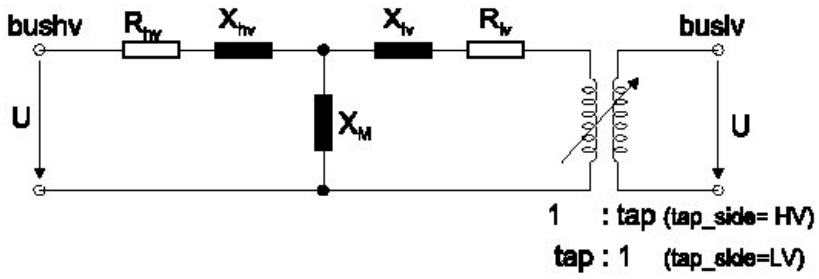

Figure 4. Transformer equivalent model. Source: DIgSILENT PowerFactory Manuals. Version 12.0 [7].

The relation between mathematical parameters in the model and parameters in the DigSilent two winding transformer type are presented on the equation set.

$$
\begin{aligned}
R_s &= R_{hv} + R_{lv} && [p.u.] \\
X_s &= X_{hv} + X_{lv} && [p.u.] \\
Z_s &= uktr/100 && [p.u.] \\
R_s &= pcutr/(1000 \cdot strn) && [p.u.] \\
X_s &= \sqrt{Z_s^2 - R_s^2} && [p.u.] \\
X_{hv} &= itrdl \cdot X_s && [p.u.] \\
X_{lv} &= (1 - itrdl) \cdot X_s && [p.u.] \\
R_{hv} &= itrdr \cdot R_s && [p.u.] \\
R_{lv} &= (1 - itrdr) \cdot R_s && [p.u.] \\
X_m &= 100/curmg && [p.u.]
\end{aligned}
$$

Figure 5. Transformer equations. Source: DIgSILENT PowerFactory Manuals. Version 12.0 [7].

DIgSILENTs zero sequence models for transformers are presented in Figure 6 and Figure 7.

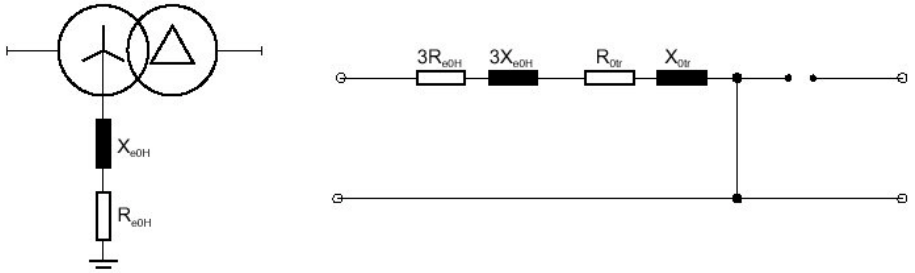

Figure 6. DIgSILENTs zero sequence model of grounded star-delta connected transformer. Source: DIgSILENT PowerFactory Manuals. Version 12.0 [7].

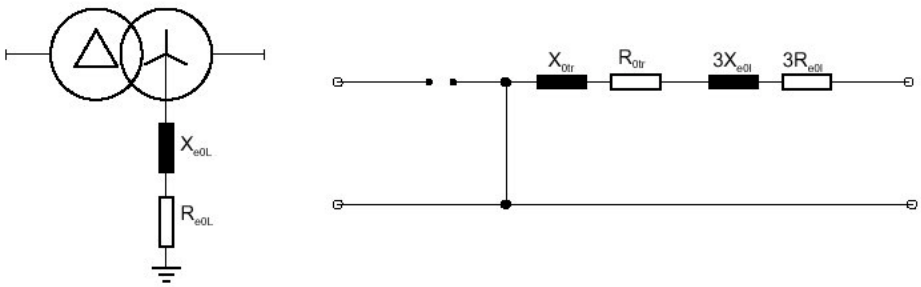

Figure 7. DIgSILENTs zero sequence model of delta - grounded star connected transformer. Source: DIgSILENT PowerFactory Manuals. Version 12.0 [7].

The relation between the parameters in the two winding transformer models and the parameters in the DIgSILENTs dialog boxes are presented on the equation set in Figure 8.

$$
\begin{aligned}
Z_0 &= uk0tr/100[p.u] \\
R_0 &= ur0tr/100[p.u] \\
X_0 &= \sqrt{Z_0^2 - R_0^2}[p.u] \\
R_{e0h} &= (re0tr_h \cdot strn)/(utrn_h^2)[p.u] \\
X_{e0h} &= (xe0tr_h \cdot strn)/(utrn_h^2)[p.u] \\
R_{e0l} &= (re0tr_l \cdot strn)/(utrn_l^2)[p.u] \\
X_{e0l} &= (xe0tr_l \cdot strn)/(utrn_l^2)[p.u]
\end{aligned}
$$

Figure 8. Relation between the parameters in the two winding transformer models and the parameters in the DIgSILENT dialog boxes. Source: DIgSILENT PowerFactory Manuals. Version 12.0 [7].

The description of the DigSilent transformer model parameters is presented in Table 1.

Table 1. DIgSILENT transformer model parameters.

strn	Rated Power
utrn_h and utrn_l	Rated voltage on HV and LV side
uktr	Short circuit voltage – positive sequence
pcutr	copper losses – positive sequence
uk0tr	Short circuit voltage – zero sequence
ur0tr	Short circuit voltage, resistive part – zero sequence
itrdl	Distribution of leakage reactances – pos. sequence
curmg	No load current
pfe	No load losses

2.2.3 Line model

The 10kV cables are modelled using the following built in DIgSILENT model shown in Figure 9.

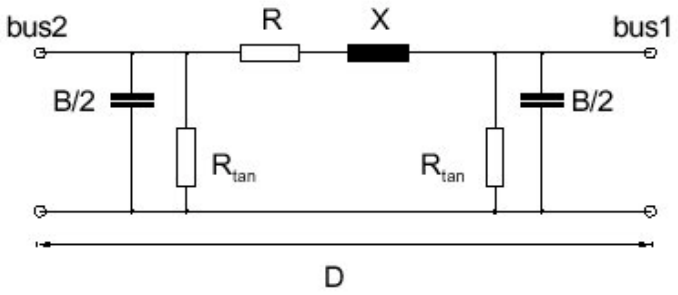

Figure 9. Transmission line model. Source: DIgSILENT

3 Grid model

The Hagesholm wind farm is connected to the 50/10 kV substation in Grevinge, which is situated 5 km from the wind farm. In the present project, the connection of the wind farm to the substation, and the substation itself are modelled by

the actual physical components, while the remaining power system is represented by simplified equivalents.

Figure 10 shows the single line diagram of the grid model, as it is printed out from DIgSILENT. The figure shows how the wind farm is connected to the substation in two groups, corresponding to the two rows shown in Figure 2. A backup line is also installed between the ends of the two lines. This backup line is normally not connected.

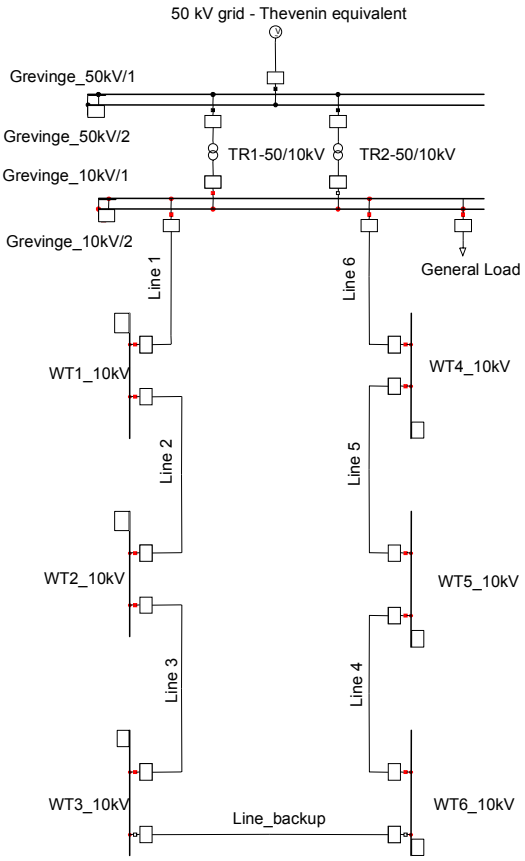

Figure 10. Single line diagram of the grid model, printed out from DIgSILENT.

The short circuit power is determined as 912 MVA, based on the 3 phase short circuit current at the 50 kV terminal provided by NVE. This is 76 times of the capacity of the wind farm, which indicates that the 50 kV grid is very strong compared to the wind farm capacity. The 50 kV grid is modelled by a Thevenin equivalent with an impedance determined by the magnitude and modulus of the 3 phase short circuit current.

In Grevinge substation, double busbars are installed on the primary side as well as the secondary side. DIgSILENT supports graphically the modelling of the possible switchings of transformers and loads provided by the double busbar structure.

The grid model is implemented using DIgSILENTs library component models, which means that the model for transformers and lines described in section 2.2 are used.

Two identical 16 MVA transformers are installed in the substation. Only one of the transformers is working in the normal operating condition. The other transformer serves as backup. The regulation of the voltage on the secondary side is assured by ± 7 tap positions of 2 % on the primary side of each transformer.

A number of load feeders are also connected to the substation in Grevinge. As a tentative solution, these loads are modelled by a single, general load directly connected to the 10 kV busbar of the substation.

4 Wind Turbine model

4.1 General

This chapter describes the wind turbine model. The wind turbine model simulates the dynamics of the system from the turbine rotor where the kinetic wind energy is converted to mechanical energy, to the grid connection point where the electric power is fed into the grid.

Each of the six wind turbines has its own wind turbine model, which enables simulation of the interaction between the wind turbines. It also makes it possible to simulate with different generator types on the individual wind turbines, as is the case in Hagesholm. Besides different generator parameters, the wind turbine models are identical. In this chapter, the model of a single wind turbine is described.

The overall structure of the wind turbine model is shown in Figure 11. It consists of an aerodynamic, a mechanical and an electric model, with an overall control system model. The electric model interfaces to the power system, represented by the grid model described in the previous chapter, whereas the aerodynamic model interfaces to the wind model described in the next chapter.

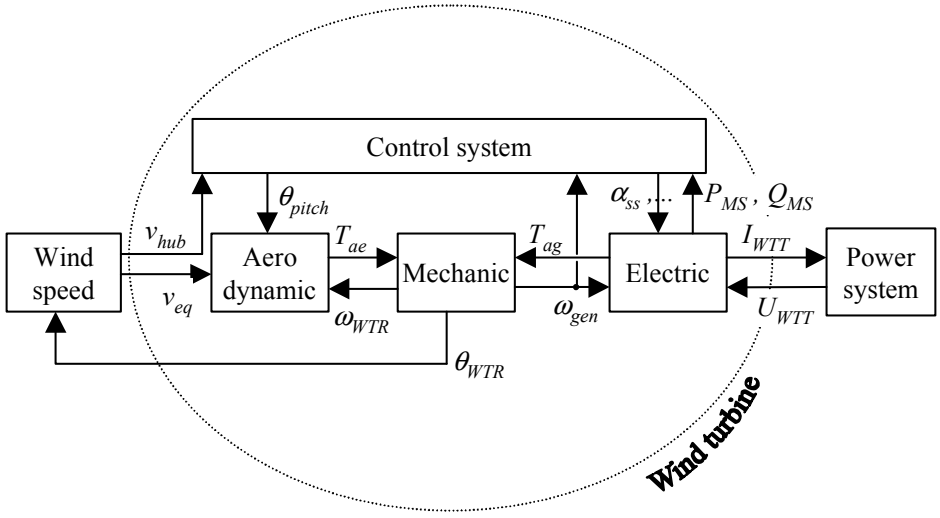

Figure 11. Overall structure of the wind turbine model, consisting of an aerodynamic model, a mechanical model and an electric model, with an overall control system model.

The electric model interfaces with the power system by the voltages U_{WTT} and currents I_{WTT} on the (10 kV) wind turbine terminals. In the other end, the electric model provides the generator air gap torque T_{ag} and uses the generator speed ω_{gen} as input. The electric model also outputs the active power P_{MS} and reactive power Q_{MS} at the main switch, representing the measured voltages and currents

of the control system. The control system provides a number of control signals for the electric model, including soft starter angle α_{ss}.

The mechanical model interfaces to the electric model as described above, and to the aerodynamic model. The inputs to the mechanical model is the aerodynamic torque T_{ae} and the air gap torque T_{ag}. The outputs are the wind turbine rotor speed ω_{WTR} and the generator speed ω_{gen}. ω_{gen} is used by the control system to control the connection of the generator through the softstarter.

The aerodynamic model uses an equivalent wind speed v_{eq}, the wind turbine rotor speed ω_{WTR} and the blade pitch angle θ_{pitch} as inputs. Its output is the aerodynamic torque T_{ae}. v_{eq} is a single wind speed time series, which represents the whole field of wind speeds in the rotor plane of the wind turbine. To include the spatial variations of the wind speed field in the rotor plane, the wind model uses the turbine rotor position θ_{WTR}, which is fed back from the mechanical model. Finally, the control system uses the wind speed measured on the nacelle, which comes from the wind model as the hub wind speed v_{hub}.

4.2 Electric model

The electric design of the NM 2000/72 wind turbine is a typical "Danish concept" with a two speed induction generator (two sets of stator windings with 4 and 6 poles respectively), a softstarter and capacitor banks for reactive power compensation.

A single line diagram of the electric model for wind turbine #1 (WT1) is shown in Figure 12. The LV/MV stepup transformer (2-WindingTransformer_t1) is placed in the nacelle because of the large size of the wind turbine. A larger wind turbine compared to a smaller wind turbine implies more power to be transmitted over a longer distance from the top of the tower to the bottom, which favours for a higher voltage in the tower cable. With that design, the tower cable becomes an MV cable rather than an LV cable, which is typically used for smaller wind turbines. Consequently, the 960 V busbar with main switch, capacitor bank (C1_t1 – C10_t1) and softstarter is also placed in the nacelle rather than in the tower bottom. Finally, the two windings in the generator is represented as two different generators, of which only one at a time is driven by the wind turbine and connected to the grid.

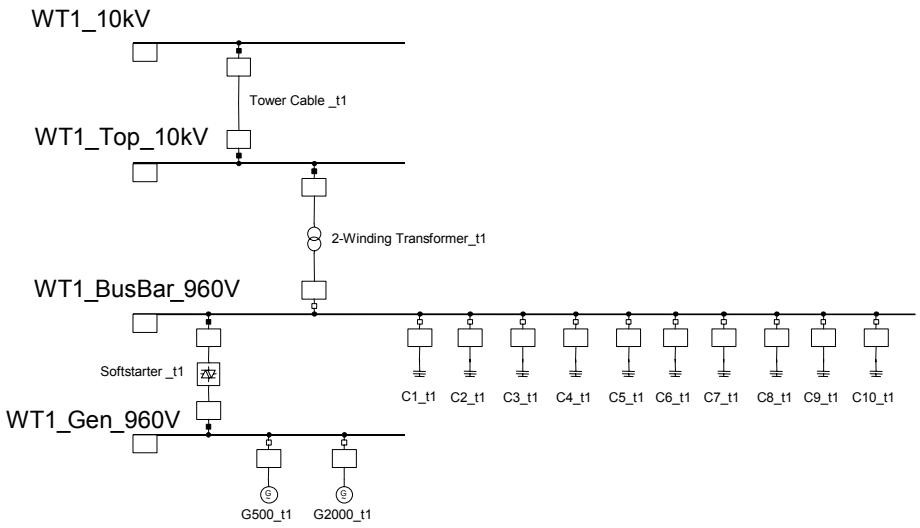

Figure 12. Single line diagram of the electric model of the wind turbine. The drawing is provided by the DIgSILENT documentation.

WT1_10kV is the wind turbine terminal to the grid in the bottom of the tower. In the simulation model, this terminal is identical to the terminal with the same name in the grid diagram Figure 10. Thus, the complete electric model of grid and wind turbines consists of one copy of Figure 10 (the grid) combined with six copies of Figure 12 (one for each wind turbine).

The electric model is implemented using DIgSILENTs library component models, i.e. the models for generators, transformers and lines described in section 2.2.

4.2.1 Capacitor bank control

As illustrated in Figure 12, the capacitor bank provides ten groups of capacitors. The first nine groups are 100 kvar, whereas the last group is 50 kvar. This design allows the reactive power compensation to switch in an interval from 0 to 950 kvar with steps of 50 kvar, which provides full load compensation of the reactive power compensation of the induction generator.

The control block controls the capacitor bank by opening and closing the connection of the capacitors in Figure 12. Figure 13 shows the composite frame of the implemented capacitor bank controller. The diagram is general for simulation of switching of capacitor banks, and consequently it can also be used to simulate other wind turbines. Only the number of steps and averaging time may differ from one wind turbine type to another.

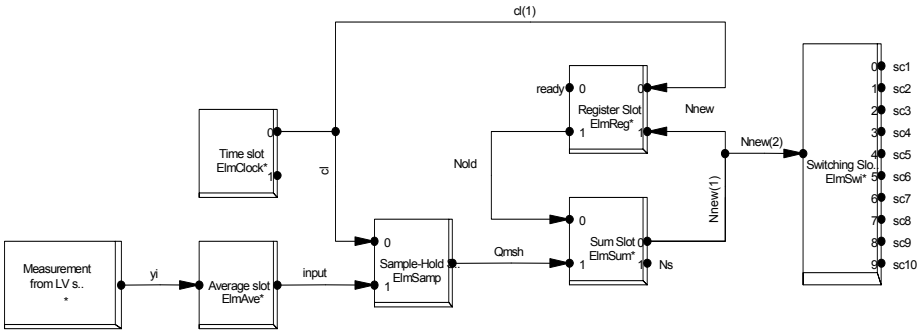

Figure 13. Composite frame for capacitor bank controller.

The first slot (Measurement from LVs..) refers to the reactive power measurement. This measurement is derived by the voltage and current measurements performed by the control system on the 2-Winding Transformer_t1 branch of the WT1_BusBar_960V in Figure 12.

The control system computer of the wind turbine averages the reactive power to stabilise the switching and to avoid that short variations in the reactive power cause switchings of the capacitors. The averaging is modelled in the simulation as in the Average slot which provides a moving average of the reactive power, succeeded by a Sample-Hold slot which converts the moving averages to block averages. The Sample-Hold slot is clocked by a Time slot with a clock frequency corresponding to the average time.

The output from the block averaging is the reactive power Qmsh. The measured reactive power includes the (closed loop) effect of the supply of reactive power from the capacitors, which are already connected. Thus, Qmsh indicates how many *additional* capacitors should be connected or disconnected.

However, for the Switching Slot, which opens and closes the connections of the capacitors, the *total* (open loop) number N of capacitors to be connected is required. N is obtained by a digital integrator, which has been implemented by a Sum slot and a Register slot. The Register slot remembers the previous number of capacitors Nold, whereas the Sum slot adds Nold to the calculated number of additional capacitors to obtain the current number of capacitors Nnew.

4.2.2 Generator model

The generator model used in this project is the build in model in DIgSILENT, described in section 2.2.1. As mentioned in section 2.1, it will be a very difficult task to implement other generator models in DIgSILENT. However, insufficient documentation and missing access to the actual code makes it difficult to evaluate and change the generator model. To evaluate the used generator model, we have implemented a model of the generator in Matlab-Simulink, and compared simulations with the DIgSILENT model to simulations with the Matlab-Simulink model. This section describes the Matlab-Simulink model, and shows a comparison of the simulations in the event of a 3 phase short – circuit.

The Matlab-Simulink model is a standard d-q model. A block diagram of the model is shown in Figure 14.

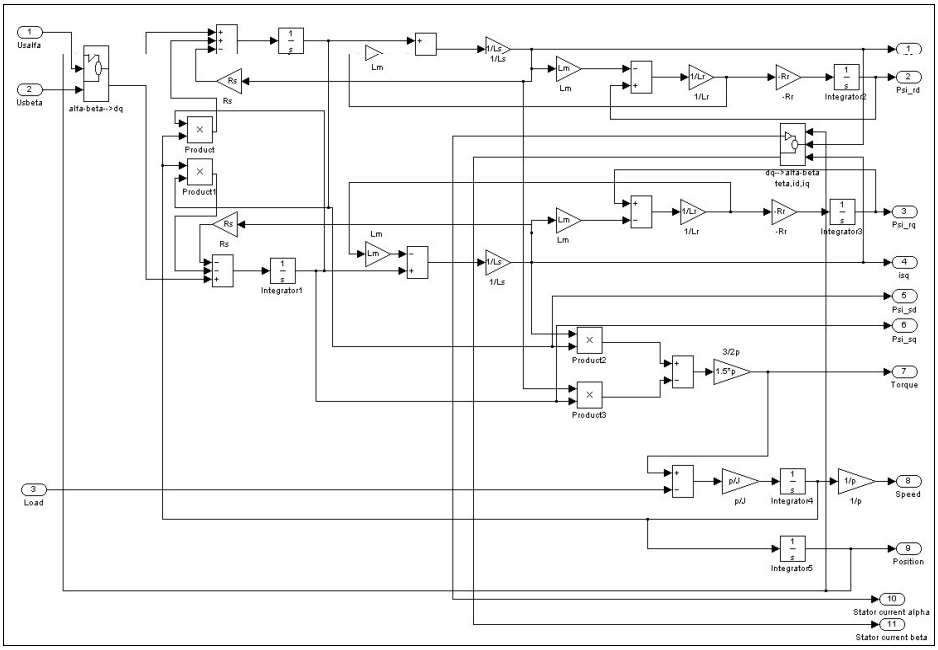

Figure 14. Induction machine d – q model in Matlab-Simulink

The equations used to build up de Matlab-Simulink induction machine d-q model are:

$$\bar{i}_s R_1 - \bar{u}_s = -\frac{d\bar{\psi}_s}{dt} - j\omega_b \bar{\psi}_s \tag{1}$$

$$\bar{i}_r R_2^{'} - \bar{u}_r = -\frac{d\bar{\psi}_r}{dt} - j(\omega_b - \omega_r)\bar{\psi}_r \tag{2}$$

$$M_e = p_1 \,\mathrm{Re}\left\{ j\bar{\psi}_s \bar{i}_s^{*} \right\} \tag{3}$$

$$\bar{\psi}_s = L_{1\sigma}\bar{i}_s + L_m\left(\bar{i}_s + \bar{i}_r\right) \tag{4}$$

$$\bar{\psi}_r = L_{2\sigma}^{'}\bar{i}_r + L_m\left(\bar{i}_s + \bar{i}_r\right) \tag{5}$$

In (1) - (5), the symbols listed in Table 2 have been used.

Table 2. Symbols used in equations (1) - (5). All the rotor quantities are transferred to the stator side.

$\bar{i}_s, \bar{i}_r$	stator and rotor current phasors
R_1 , R_2'	stator and rotor resistances
$\bar{u}_s, \bar{u}_r$	stator and rotor voltage phasors
$\bar{\psi}_s, \bar{\psi}_r$	stator and rotor flux phasors
ω_b	angular velocity of the reference system
ω_r	angular velocity of rotor
M_e	electric torque
p_1	number of pole pairs
$\mathrm{Re}\{x\}$	real part of x
$\bar{x}^*$	complex conjugated of $\bar{x}$
$L_{1\sigma}$, $L_{2\sigma}$'	stator and rotor leakage inductances
L_m	mutual inductance

To demonstrate the Matlab-Simulink model, simulation results are presented in Figure 15 for the induction generator which is used in wind turbine #1. What is simulated is the imaginary event of a full load startup of the generator from stand still, which causes high transient currents as can be studied in text book. The case is not representative for the behaviour of a wind turbine, because it connects the generator about rated rotor speed, and with a softstarter to limit the currents, but the simulations can be compared to text book studies.

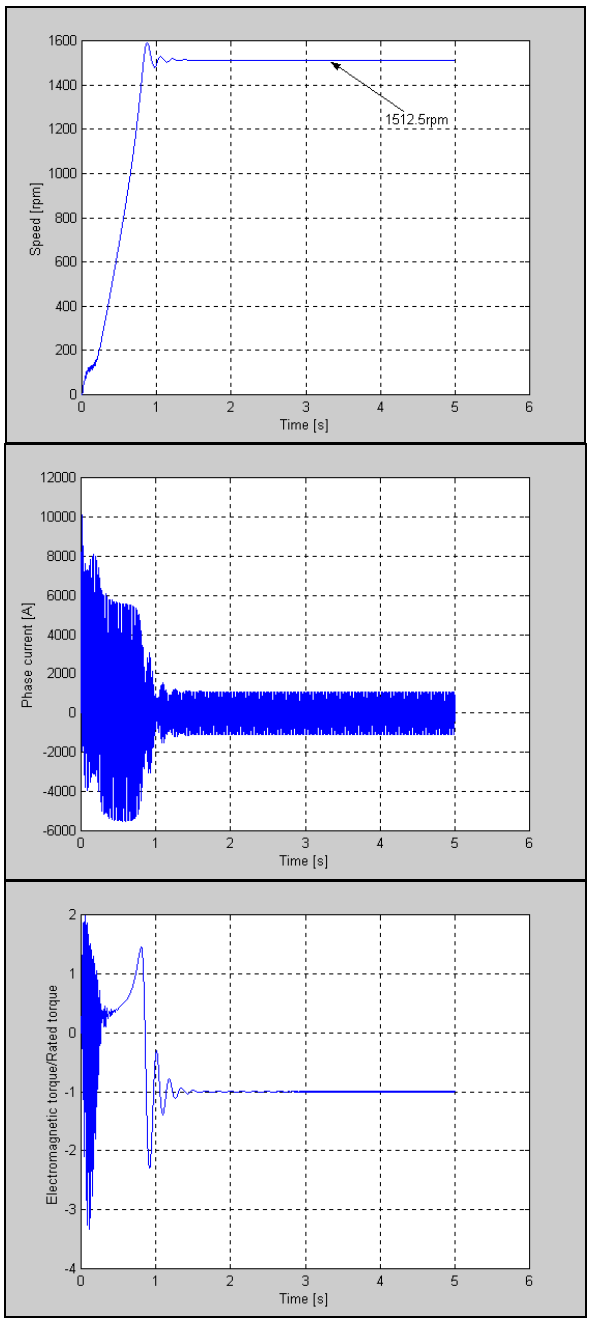

Figure 15. Speed, current and torque transients during the imaginary event of generator full load startup from stand still, simulated with the Matlab-Simulink model. The simulations demonstrate the dynamics of the generator, but the simulated transients will not occur in real wind turbine operations, because the generators in real operation are connected near rated speed and through a softstarter to limit the current transients.

For comparison of the Matlab–Simulink model to the DIgSILENT model, a three-phase short-circuit at generator terminals at nominal operation point has been simulated with both models. The simulations are done with pure generator models, and consequently, they do not provide information about, how the wind turbines would behave in the event of a short-circuit.

The simulation results are presented in Figure 16. These comparative results show a good similarity between a custom d – q Matlab model and DigSilent built in model of the induction machine for transient simulations.

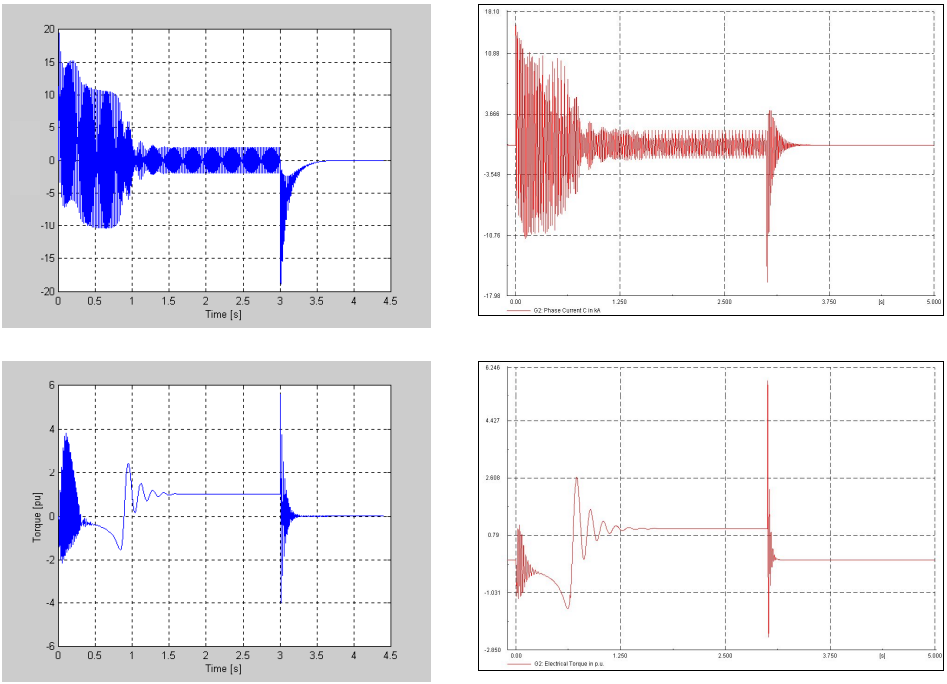

Figure 16. Comparison of simulations of phase current and electromagnetic torque transients for a 3 phase shrot-circuit. The first column is with Matlab-Simulink model, and the second column is with the DIgSILENT model.

The above comparisons are based on DIgSILENT simulations with the single-cage rotor, see Figure 3. That rotor model is equivalent to the one implemented in the Matlab-Simulink model.

For the remainder simulations presented in this report, DIgSILENTs generator model with a squirrel-cage rotor is applied. According to DIgSILENT, this model provides a more realistic torque curve outside the linear area, because the model considers the rotor current displacement in squirrel cage rotors.

4.3 Mechanical model

The mechanical model is selected with emphasis to include only the parts of the dynamic structure of the wind turbine, which are important to the interaction with the grid, i.e. which influences significantly on the fluctuations of the power. Thus, only the drive train is considered in the first place because this part of the wind turbine has the most significant influence on the power fluctuations.

The mechanical model is illustrated in Figure 17. The aerodynamic torque T_{ae} is provided by the aerodynamic model as illustrated in Figure 11, and the wind turbine rotor angle θ_{WTR} (Figure 17) derived provides the rotor speed ω_{WTR} (Figure 11). On the other side in Figure 11, the mechanical model interfaces to the generator model with the air gap torque T_{ag} and the generator speed ω_{gen} which is derived from the generator angle position θ_{gen}.

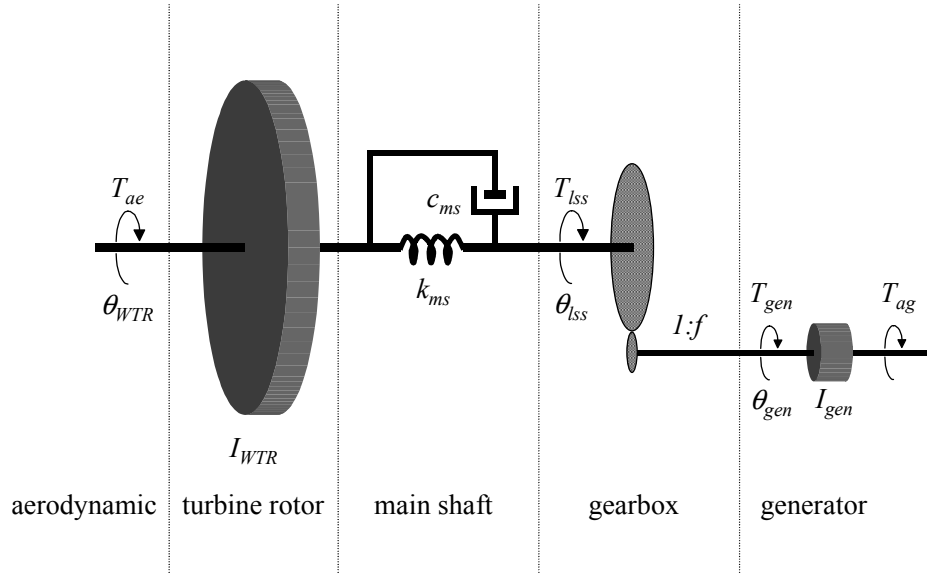

Figure 17. Mechanical model for the wind turbine. The model only includes the drive train, because this part of the wind turbine has the most significant influence on the power fluctuations.

The drive train model is essentially a two mass model. The masses used in the model correspond to a large turbine rotor inertia I_{WTR} representing the blades and hub, and a small inertia I_{gen} representing the induction generator.

The mechanical model of the turbine rotor, main shaft and gearbox is implemented in DIgSILENTs DSL environment, whereas the generator inertia I_{gen} is included in DIgSILENTs generator model. I_{gen} is specified through the "acceleration time constant" T_{aG} given by

$$T_{aG} = \frac{2H}{\cos \varphi} \tag{6}$$

where H is the inertia constant given by

$$H = \frac{1}{2} \frac{I\omega_{gen,n}{}^2}{S_{gen,n}} \tag{7}$$

In (7), $\omega_{gen,n}$ is the rated generator rotor speed in rad/s and $S_{gen,n}$ is the rated apparent power of the generator. In standard applications, the inertia I includes the generator as well as the turbine, but as the turbine inertia I_{WTR} is included in the DSL part of our model, only the generator inertia I=I_{gen} is used in (7), when T_{aG} for the generator model is calculated according to (6). This approach has been verified by test runs with different turbine inertia's I_{WTR} and acceleration time constants T_{aG}. Simple mechanical calculations on the simulation results before the generator is connected to the grid verify that the sum of the inertia I in (7) and I_{WTR} in the DSL model determines the acceleration of the generator.

The flexibility of the shaft is modelled as a stiffness k_{ms} and a damping c_{ms}. Moreover, an ideal gear with the exchange ratio *1:f* is included in the model. The stiffness and damping components are modelled on the low speed shaft, but flexibility in the gear and on the high speed shaft can also be included here, if they are corrected for the gear ratio.

As mentioned above, I_{gen} is integrated in the generator model. The remaining part of the mechanical model is implemented as state space equations in DIgSILENTs DSL. The input variables $\overline{u}$ for this part of the model are

$$\bar{u} = \begin{pmatrix} \omega_{gen} \\ T_{ae} \end{pmatrix} \tag{8}$$

and the output variables $\bar{y}$ are

$$\bar{y} = \begin{pmatrix} T_{gen} \\ \theta_{WTR} \\ \omega_{WTR} \end{pmatrix} \tag{9}$$

We select the states

$$\bar{x} = \begin{pmatrix} \theta_k \\ \theta_{WTR} \\ \omega_{WTR} \end{pmatrix} \tag{10}$$

where θ_k is the angular difference between the two ends of the flexible shaft, i.e.

$$\theta_k = \theta_{WTR} - \theta_{lss} = \theta_{WTR} - \frac{\theta_{gen}}{f} \tag{11}$$

Then we obtain the state space equations

$$\dot{\bar{x}} = \begin{pmatrix} 0 & 0 & 1 \\ 0 & 0 & 1 \\ -\frac{k_{ms}}{I_{WTR}} & 0 & -\frac{c_{ms}}{I_{WTR}} \end{pmatrix} \cdot \bar{x} + \begin{pmatrix} \frac{1}{f} & 0 \\ 0 & 0 \\ \frac{c_{ms}}{f \cdot I_{WTR}} & \frac{1}{I_{WTR}} \end{pmatrix} \cdot \bar{u} \tag{12}$$

$$\bar{y} = \begin{pmatrix} \frac{k_{ms}}{f} & 0 & \frac{c_{ms}}{f} \\ 0 & 1 & 0 \\ 0 & 0 & 1 \end{pmatrix} \cdot \bar{x} + \begin{pmatrix} -\frac{c_{ms}}{f^2} & 0 \\ 0 & 0 \\ 0 & 0 \end{pmatrix} \cdot \bar{u} \tag{13}$$

Instead of the damping coefficient c_{ms}, the logarithmic decrement δ_{ms} is often used to characterise the damping. The damping coefficient can be obtained from the logarithmic decrement according to

$$c_{ms} = 2 \cdot \delta_{ms} \cdot \sqrt{\frac{k_{ms} \cdot I_{WTR}}{{\delta_{ms}}^2 + 4\pi^2}} \tag{14}$$

4.4 Aerodynamic model

The aerodynamic model outputs the aerodynamic torque T_{ae} to the mechanical model, as can be seen in Figure 11. The inputs to the aerodynamic model are the equivalent wind speed v_{eq} from the wind model, the turbine rotor speed ω_{WTR} from the mechanical model and the pitch angle θ_{pitch} from the control system. Thus, the aerodynamic model supports variable speed as well as blade angle control.

Aerodynamic models are used in simulation programs for structural design of wind turbines, which are used by the wind turbine industry, developers, research institutes etc. The aerodynamic models in these programs typically use blade

element iteration to predict the aerodynamic loads on sections of each blade. These loads are then integrated up on each blade to provide the loads on e.g. the shaft.

The blade element iteration consumes considerable computer time. Although only six wind turbines are simulated in the present project, the idea with the model is to be able to use it to simulate a wind farm with maybe hundreds of wind turbines in the future. Therefore, each wind turbine model should be reduced to include only the most significant effects on the power.

Therefore, the present aerodynamic model is based on the aerodynamic efficiency C_p. The idea is first to calculate C_p with a standard aerodynamic program which uses blade element iteration, and then use the calculated C_p values as an input table for the simulation. This simplification is not sufficient for structural load programs, because these programs simulate many other loads than the aerodynamic torque.

For a given wind turbine rotor, C_p depends on the tip speed ratio λ and the blade pitch angle θ_{pitch}, i.e. $C_p = C_p(\lambda, \theta_{pitch})$. λ is defined as the ratio between the blade tip speed and the wind speed, i.e. with a blade radius R, λ is defined as

$$\lambda = \frac{\omega_{WTR} \cdot R}{v_{eq}} \tag{15}$$

This means that C_p can be tabled as a matrix by the aerodynamic program, and used in this code. Using C_p, the aerodynamic power P_{ae} determined by

$$P_{ae} = \frac{1}{2} \rho \pi R^2 \, v_{eq}{}^3 \, C_p \tag{16}$$

where ρ is the air density. Combining (15) and (16), the aerodynamic torque T_{ae} is determined directly by the aerodynamic power according to

$$T_{ae} = \frac{P_{ae}}{\omega_{WTR}} = \frac{\pi}{2\lambda} \rho R^3 \, v_{eq}{}^2 \, C_p \tag{17}$$

This method corresponds to the steady state aero loads, which are also reflected in the power curve. However, such a simplification underestimates the power fluctuations in the stall region. As indicated by the flat power curve in the stall region, large wind speed fluctuations will only imply small power fluctuations. However, due to dynamic stall effects, the actual power fluctuations are much higher.

Therefore, a model for dynamic stall was included. The applied model for dynamic stall is based on Øye's dynamic stall model [10]. Øye's simulates dynamic stall as time lag of separation, and implements the time lag directly on the lift coefficients used by the blade element iteration in the individual blade sectors. This approach is not possible in our case, because we base the aerodynamic model on a C_p table.

To include the dynamic stall effect in the model, and keep it C_p based, we have implemented a time lag on C_p, which is similar to Øyes time lag on the lift coefficients.

Øyes procedure first uses the static lift coefficients to determine a lift coefficients for unseparated and separated flow respectively. We have done the same as shown in Figure 18. The lift coefficient for unseparated flow is determined as the theoretical value with the slope 2π and the same zero crossing as the static lift coefficient. The lift coefficient for separated flow is determined to fit the static curve for high angles of attack

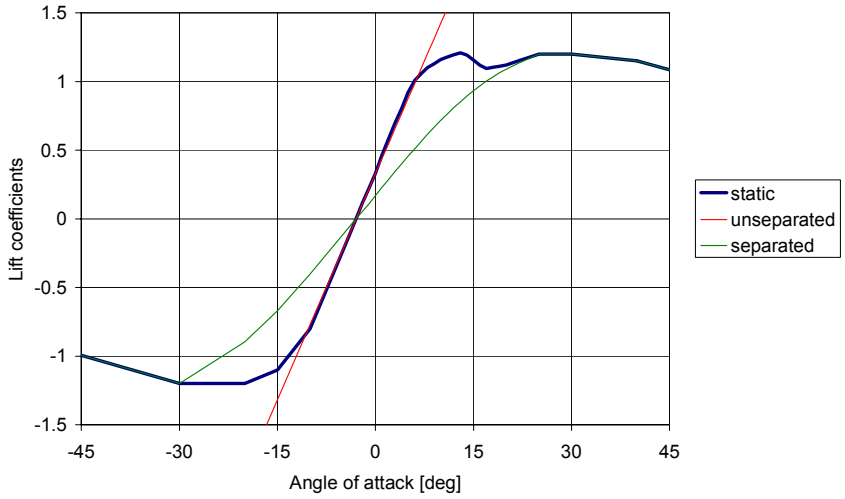

Figure 18. Lift coefficients for static flow is used to generate lift coefficients for unseparated and separated flow, respectively.

Then we have used these two additional lift curves to generate two additional C_p tables $C_{p,sep}$ and $C_{p,unsep}$ with the aerodynamic program, which we have already used to calculate the $C_{p,st}$ table for steady state. Then our model implements a time delay corresponding to a time constant τ on the C_p values instead of the lift coefficients. The delay is implemented as follows:

1. Use the instantaneously relevant elements in the three C_p tables to determine f_{st} as the static value of the "ratio of unsaparation", i.e. from the equation

$$C_{p,st} = f_{st} \cdot C_{p,unsep} + (1 - f_{st}) \cdot C_{p,sep} \tag{18}$$

2. Low pass filter the static ratio of unseparation f_{st} to obtain dynamic ratio of unseparation f using the differential equation

$$\frac{df}{dt} + \frac{(f - f_{st})}{\tau} = 0 \tag{19}$$

3. Calculate the dynamic value of C_p from

$$C_p = f \cdot C_{p,unsep} + (1 - f) \cdot C_{p,sep} \tag{20}$$

4. The dynamic value of C_p is then used to determine the aerodynamic torque according to (17).

The above procedure is almost equivalent to Øyes procedure. This can be seen by the curves in Figure 19. Besides the C_p curves for steady state, separated flow (f=0.00) and unseparated flow (f=1.00), the C_p curves for different f values have been calculated with the aerodynamic program.

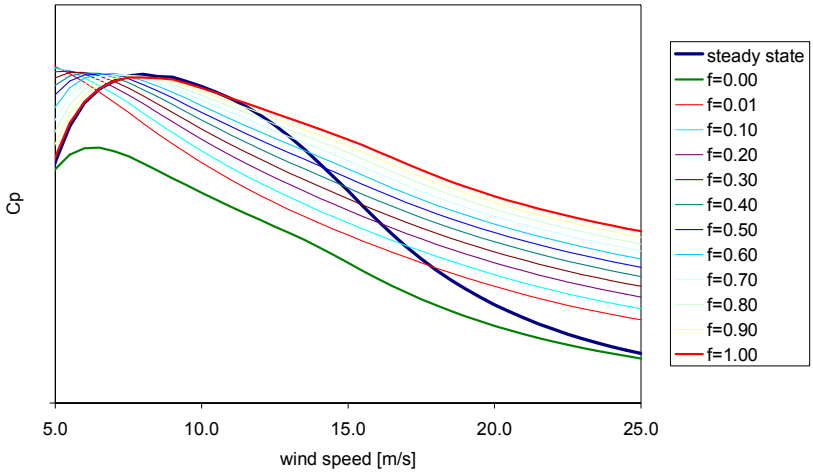

Figure 19. C_p curves for static flow and for different "degrees of unseparation" f.

It can be seen that the methods are equivalent for wind speeds above 10 m/s in the following way: In Øyes case, the instantaneous response to wind speed changes is to follow the iso-f curve, and after the delay to come back to the steady state curve. In our case, the instantaneous response is to follow a curve with constant interpolation ratio between the f=0.00 and f=1.00 curves, and after the delay to come back to the steady state curve. It is seen from the figure that the iso-f curves are very close to curves which would be generated as interpolations between the f=0.00 and f=1.00 curves. Therefore the instantaneous response to wind speed changes will be almost identical with the two models.

The described procedure also works properly below 10 m/s. In that wind speed range, the steady-state curve is close to the unseparated curve, i.e. $f \approx 1$. Consequently, the instantaneous response will almost be equal to the steady state response, so the dynamic stall procedure will behave as a steady-state procedure below 10 m/s. This is convenient, because it allows the simulations to use the dynamic stall procedure in the whole wind speed range.

5 Wind model

5.1 General

The wind model is essential to obtain realistic simulations of the power fluctuations during continuous operation of the wind farm. The wind model combines the stochastic effects caused by the turbulence and deterministic effects caused by the tower shadow. The stochastic part includes the (park scale) coherence between the wind speeds at different wind turbines as well as the effects of rotational sampling, which is known to move energy to multiples (often denoted p's, e.g. 3p) of the rotor speed from the lower frequencies [11]. The park scale model does not include the effects of wakes from the wind turbines, but the mean wind speed and turbulence intensity can be modified to account for these effects.

Only the longitudinal component of the wind speed is included in the model, which is normally a reasonable assumption for wind turbines, because this component has the dominating influence on the aero loads on wind turbines.

The park scale coherence is included, because it ensures realistic fluctuations in the sum of the power from each wind turbine. This is important for the maximum power output from the wind farm in e.g. a 10 minutes period.

In IEC 61400-21 [3], it is specified that the maximum 200 ms average power $P_{0.2}$ as well as the maximum 1 minute average power P_{60} must be measured as a part of the power quality test of wind turbines.

To be able to extend the results from measurement of $P_{0.2}$ on a single wind turbine to a wind farm with N_{wt} wind turbines, IEC 61400-21 assumes that the fluctuating part of the 200 ms average power of the i^{th} wind turbines is uncorrelated with 200 ms average power of the other wind turbines. Moreover, it is assumed that for each wind turbine i, the maximum 200 ms power $P_{0.2,i}$ appear a rated power $P_{n,i,}$. These assumptions leads to the following estimate of the maximum 200 ms power $P_{0.2\Sigma}$ of a wind farm with N_{wt} wind turbines

$$P_{0.2\Sigma} = \sum_{i=1}^{N_{wt}} P_{n,i} + \sqrt{\sum_{i=1}^{N_{wt}} \left(P_{0.2,i} - P_{n,i}\right)^2} \tag{21}$$

Likewise, to be able to extend the results from measurement of P_{60} on a single wind turbine to a wind farm with N_{wt} wind turbines, IEC 61400-21 assumes that the fluctuating part of the 60 s average power of the i^{th} wind turbines is fully correlated, i.e. identical to the 60 s. average power of the other wind turbines. This assumptions leads to the conservative estimate of the maximum 60 ms power $P_{60\Sigma}$ of a wind farm with N_{wt} wind turbines given by the simple summation

$$P_{60\Sigma} = \sum_{i=1}^{N_{wt}} P_{60,i} \tag{22}$$

(21) and (22) are both approximations, which reflects that the fast fluctuations are almost uncorrelated, while the slow fluctuations are more correlated. However, a more detailed stochastic model, which takes into account the varying coherence over the whole frequency range, will be able to predict the summation effects more accurately.

Assuming that the fast wind speed fluctuations are uncorrelated, a corresponding relation can be made to predict the standard deviation of the power from a wind farm, knowing the standard deviation of the power from each wind turbine. However, analyses of measurements, e.g. Tande et.al. [12], have shown that the assumption of uncorrelated distributions implies an underestimation of the standard deviation of the power from a wind farm.

The main reason for this underestimation is assumed to be the influence of the actual correlation between the wind speeds in the wind farm, which is particularly strong when the distance between the wind turbines is small. The present wind speed model includes the correlation in terms of the coherence between the wind speeds to be able to obtain better estimates of maximum power and power standard deviation.

The effect of the rotational sampling is included because it is a very important source to the fast power fluctuations during continuous operation of the wind turbine. In many cases, e.g. Sørensen [13], measurements have shown that the 3p effect due to rotational sampling provides the main effect to flicker during continuous operation.

The structure of the wind model used in this project is shown in Figure 20. It is built as a two step model. The first step is the park scale wind model, which simulates the wind speeds $v_{hub,1}$ - $v_{hub,N}$ in a fixed point (hub heigh) at each of the

N wind turbines, taking into account the park scale coherence. The second step is the rotor wind model, which provides an equivalent wind speed $v_{eq,i}$ for each wind turbine i, i.e. a single time series for each wind turbine, which is used as input to the aerodynamic model of that wind turbine.

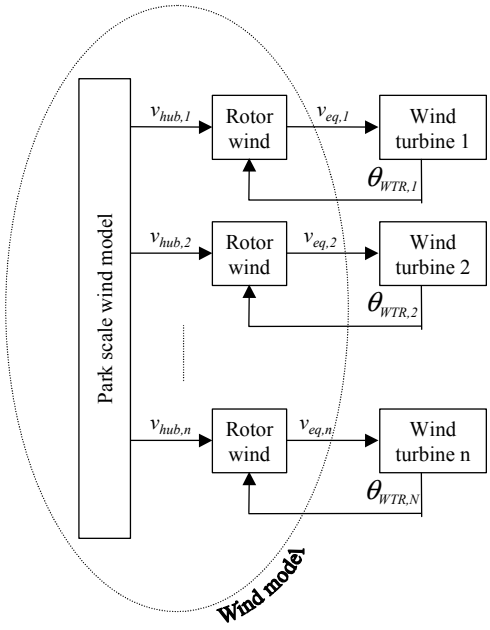

Figure 20: Structure of wind model.

The park scale wind model is implemented in an external program PARKWIND that generates a file with hub wind speed time series, which are then read by DIgSILENT. This is possible because the wind speeds are assumed to be independent on the operation of the wind farm, which is reasonable because the required wind speed $v_{hub,i}$ for each wind turbine i is the wind speed in hub height if wind turbine i was not erected.

The present version of PARKWIND is based on user inputs of the expected mean wind speeds and turbulence intensities at the wind turbines. Modifying these parameters, the effects of terrain roughness and wind turbine wakes can be included in the simulations. For a given terrain with a given mean flow, the ambient mean wind speeds and turbulence intensities at the individual wind turbine positions can be determined using Risøs computer program WAsP Engineering [14]. Furthermore, the effects of wakes in the wind farm can be included, e.g. using Jensens [15] suggested wind farm model to predict the reduction of the mean wind speed in a wake, and Frandsen and Thøgersen's model [16] for combining the ambient turbulence and the wake induced turbulence. The wake effects may be included in future versions of WAsP Engineering, so that WAsP Engineering can be used directly to determine the necessary input parameters for the simulations with the PARKWIND code.

The rotor wind models describes the influence of rotational sampling of the wind turbine blades over the whole rotor plane. The model for the wind field includes turbulence as well as tower shadow effects. These effects are included for each of the n wind turbines individually. The wind speed seen by the rotating blades depends on the azimuth position $\theta_{WTR,i}$ of the wind turbine rotors. As illustrated in Figure 11, $\theta_{WTR,i}$ is fed back from the mechanical part of the wind turbine model.

The wind model provides an equivalent wind speed $v_{eq,i}$ for each wind turbine i, which is used as input to the aerodynamic model of that wind turbine. $v_{eq,i}$ is a single time series for the wind turbine i, which takes into account the variations in the whole wind speed field over the rotor disk. The advantage of using the

equivalent wind speed is that it can be used together with a simple, C_p based aerodynamic model, and still include the effect of rotational sampling of the blades over the rotor disk [17].

5.2 Park scale model

5.2.1 Review of methods

Different methods can be applied to simulate the wind speeds in a wind farm. Estanqueiro [18] used the Shinozuka method [19] based on a cross spectral matrix. Initially, Manns [20] simulation method was suggested used in this project, because the calculation speed of the method is generally faster than cross spectral matrix method. Some of the results using Manns model were presented in Sørensen et.al. [21].

Both Estanqueiro use of the Shinozuka method and the Mann method assume Taylors frozen turbulence hypothesis illustrated for a two-dimensional wind speed field in Figure 21. The wind speed field is generated in spatial dimensions in the first place, and then the turbulence field is moved forward with the mean wind speed.

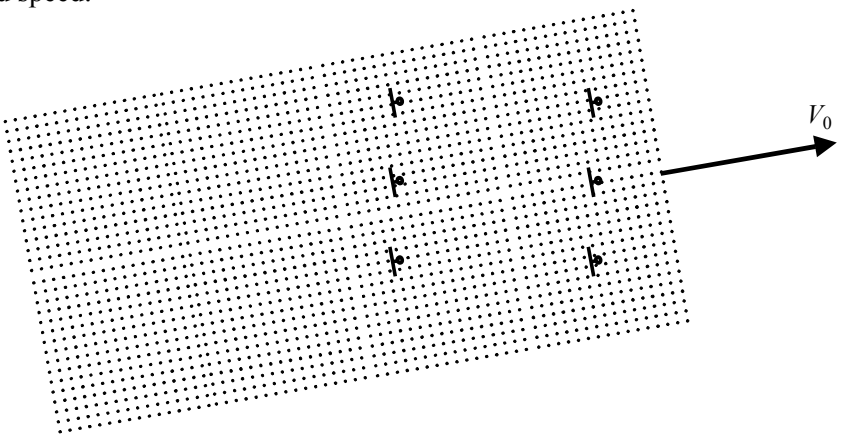

Figure 21. Simulation of park scale wind speeds with the assumption of Taylors frozen turbulence hypothesis.

Taylors frozen turbulence hypotheses is a reasonable assumption for simulations where the simulated time series only pass the object once, like a wind turbine rotor. Methods assuming Taylors hypotheses are therefore used in computer programs for simulation of mechanical loads on wind turbines to simulate the wind speed variations in the rotor plane of a single wind turbine. One example is Veers [22] use of Shinozukas cross spectral method, another example is Manns method. In these cases, the simulated wind speed time series only pass the object once.

But for park scale wind simulations, the Taylor hypothesis is not realistic, especially when the wind direction is along a line of wind turbines. In that case, simulations assuming Taylors frozen turbulence will generate wind speed time series with full coherence between the wind speeds at the wind turbines in the line. This is not realistic, and it will significantly effect the summation of power fluctuations from the wind turbines in that line.

5.2.2 The complex cross spectral method

To avoid the assumption of Taylors frozen turbulence, we have developed a new method for simulation of park scale wind speeds. The new method is im-

plemented as the software code PARKWIND. It is based on Shinozukas cross spectral matrix method, using a complex cross spectral matrix instead of the real cross spectral matrix, which is used with Taylors frozen hypotheses. The complex matrix introduces the phase angles representing the delay between points with a longitudinal distance.

The complex cross spectral method also has the advantage that it does not produce more data than what is needed. The Mann method on the other hand produces a grid of data, which then in turn has to be interpolated in at the initial positions of the wind turbines relative to the grid. The complex cross spectral method directly generates a single time series at the position of each wind turbine. Because of the data reduction, the new method also reduces the computation time considerably compared to the fast Mann method.

To explain the PARKWIND method, the cross spectral method will also be described here. The cross spectral method is based on the cross power spectrum matrix $\boldsymbol{S}(f)$, which with N points (corresponding to a wind farm with N wind turbines) is an $N \times N$ matrix. We have chosen to use the frequency in Hz, f. Each element $S_{rc}(f)$ in row r, column c of $\boldsymbol{S}(f)$ is determined as the cross power spectrum between point number r and point number c.

$S_{rc}(f)$ is defined as the Fourier transform of the cross correlation function $R_{rc}(\tau)$ according to

$$S_{rc}(f) = \int_{-\infty}^{\infty} R_{rc}(\tau) e^{-j2\pi f\tau} d\tau \tag{23}$$

The cross correlation function $R_{rc}(\tau)$ between $v_{hub,r}(t)$ and $v_{hub,c}(t)$ is defined as

$$R_{rc}(\tau) = E\{v_{hub,r}(t) \cdot v_{hub,c}(t-\tau)\} \tag{24}$$

where $E\{f(t)\}$ denotes the mean value of $f(t)$ over the time t and τ is the delay time.

The first step in the cross power spectral method is to determine $S_{rc}(f)$. Figure 22 shows the two points r and c. The distance between the two wind turbines is d_{rc}, with the angular direction θ_{rc} from north. The mean wind speed V_0 and the wind direction θ_V are also shown. $\alpha_{rc} = \theta_V - \theta_{rc}$ is the inflow angle.

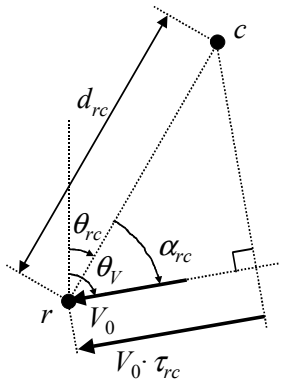

Figure 22. Two points r and c each corresponding to a wind turbine. The distance between the two points r and c is d_{rc}, with a direction θ_{rc} from north. V_0 is the mean wind speed, and θ_V is the wind direction. α_{rc} is the resulting inflow angle, and τ_{rc} is the delay time.

Figure 22 also indicates the delay time τ_{rc} for the wind field to travel from wind turbine c to wind turbine r. Simple geometry yields τ_{rc} determined as

$$\tau_{rc} = \frac{\cos(\alpha_{rc}) \cdot d_{rc}}{V_0} \tag{25}$$

To represent the time delay τ_{rc} in the cross power spectrum, we assume that $R_{rc}(\tau)$ as defined in (24) is symmetric about τ_{rc}. Then using (23), it can be shown that the complex angle of $S_{rc}(f)$ is $-2\pi f\tau_{rc}$, i.e.

$$S_{rc}(f) = |S_{rc}(f)| \cdot e^{-j2\pi f\tau_{rc}} \tag{26}$$

The magnitude of the cross power spectrum $|S_{rc}(f)|$ can be determined using the standard definition of the coherence function $\gamma^2(f,d,V_0)$,

$$\gamma^2(f, d_{rc}, V_0) = \frac{|S_{rc}(f)|^2}{S_{rr}(f)S_{cc}(f)} \tag{27}$$

Combining (27) and (26), we can express the complex cross power spectrum as

$$S_{rc}(f) = \gamma(f, d_{rc}, V_0)\sqrt{S_{rr}(f)S_{cc}(f)} \cdot e^{-j2\pi f\tau_{rc}} \tag{28}$$

The second step is to discretise the frequency to be able to represent the spectra in a numeric computer code. Simulating time series with the period length T_P, the frequency f is discretised in steps $\Delta f = 1/T_P$., i.e. the i^{th} frequency $f[i]=i\cdot\Delta f$. The corresponding discrete value of $S_{rc}(f)$ is $S_{rc}[i]= S_{rc}(f_i)\cdot\Delta f$.

We also discretise the time, using the sampled representation of the wind speeds as time series with time steps $\Delta t=1/f_s$, where f_s is the sampling frequency in Hz. This sampling limits the frequency to $\pm f_s/2$ and consequently the frequency index i to $\pm N_s/2$, where

$$N_s = T_P \cdot f_s \tag{29}$$

is the number of samples in the simulated time series. Obviously, N_s must be an integer, and preferably an exponent of 2 which enables the use of an FFT to speed up the Fourier transformation used in the end of the method. This can be obtained by adjusting either T_P or f_s according to (29).

Selecting an appropriate sampling frequency and assuming two-sided spectra, this discretisation ensures that the variance σ_r^2 of the wind speed at wind turbine r is preserved according to

$$\sigma_r^2 = \int_{-\infty}^{\infty} S_{rr}(f)df \approx \int_{-f_s/2}^{f_s/2} S_{rr}(f)df \approx \sum_{i=-N_s/2}^{N_s/2} S_{rr}[i] \tag{30}$$

The discretisation is only done for frequency indices $i\geq 0$, because the values for $i<0$ are given by $S_{rc}[-i]= S_{rc}^*[i]$, where * denotes complex conjugation.

The third step is for each frequency index $i\geq 0$ to resolve the discrete matrix $\boldsymbol{S}[i]$ with the elements $S_{rc}[i]$ into a product of the transformation matrix $\boldsymbol{H}[i]$ and the transpose of its conjugate $\boldsymbol{H}^{*T}[i]$, i.e.

$$\boldsymbol{S}[i] = \boldsymbol{H}[i]\boldsymbol{H}^{*T}[i] \tag{31}$$

Choosing the solution where $\boldsymbol{H}[i]$ is a lower triangular matrix, i.e. the element $H_{rc}[i]=0$ if $c>r$, it can be shown that this is done element by element. The diagonal elements are determined according to

$$H_{rr}[i]=\sqrt{S_{rr}[i]-\sum_{k=1}^{r-1} H_{rk}[i]H_{rk}^*[i]} \tag{32}$$

and the elements below the diagonal are determined according to

$$H_{rc}[i]=\frac{S_{rc}[i]-\sum_{k=1}^{c-1} H_{rk}[i]H_{ck}^*[i]}{H_{cc}[i]} \tag{33}$$

It can be seen from (32) and (33) that $\boldsymbol{H}[i]$ gets the same phases as $\boldsymbol{S}[i]$, i.e. zero phase shift in the diagonal and a phase shift $-2\pi f\tau_{rc}$, below the diagonal, corresponding to the delay of the wind speed between two wind turbines r and c.

The fourth step is for each frequency index $i \geq 0$ to generate an $N \times 1$ vector $\boldsymbol{E}[i]$ of unity complex numbers with a random phase. This is done by simulating N random phase angles $\varphi_r[i]$ using a random generator with uniform distribution in the interval $[0;2\pi]$, and calculate each element E_r in row r of $\boldsymbol{E}$ according to

$$E_r = e^{j\varphi_r[i]} \tag{34}$$

The fifth step is for each frequency index $i \geq 0$ to calculate a vector $\boldsymbol{V}_{hub}[i]$ containing the i^{th} Fourier coefficients of all N wind speed time series according to

$$\boldsymbol{V}_{hub}[i] = \boldsymbol{H}_{hub}[i]\boldsymbol{E}[i] \tag{35}$$

The imaginary part of $\boldsymbol{V}_{hub}[0]$ should be set to zero, because $\boldsymbol{V}_{hub}[-i] = \boldsymbol{V}_{hub}[i]^*$ and consequently and consequently $\boldsymbol{V}_{hub}[0] = \boldsymbol{V}_{hub}[0]^*$, which is only possible if $\boldsymbol{V}_{hub}[0]$ is real.

Finally, for each wind turbine r, the Fourier coefficients are joined in an array $V_{hub,r}$, and an inverse Fourier transform is performed to obtain the time series $v_{hub,r}(t)$.

5.2.3 Spectral distributions

In its present state, the model is capable of simulating wind speeds with power spectra of either Kaimal or Højstrup type, but implementation with another spectrum is straightforward, as the spectra are only used explicitly according to (28). The Kaimal spectrum has been selected in the first place because it is used widely, while the Højstrup spectrum was selected because it includes more energy than the Kaimal spectrum at the low frequencies, and this has shown to agree better in a number of cases. The lower frequencies are particularly important for the summation effects, because the coherence is highest for lowest frequencies.

The two-sided Kaimal spectrum [23] $S_{Kai}(f)$ can be written as

$$S_{Kai}(f) = u_*^2 \frac{2.4\,\dfrac{L}{V_0}}{\left(1 + 1.5\,\dfrac{L}{V_0}\,f\right)^{5/3}} \tag{36}$$

In (36), we have used the length scale $L=22z$, where z is the height. This substitution has been made because the original Kaimal spectrum dependence on the height z is only valid in the lower boundary layer ($z<30$m), i.e. in (36) and (39), we will assume

$$L = \begin{cases} 20z & \text{for } z < 30\text{m} \\ 600\text{m} & \text{otherwise} \end{cases} \tag{37}$$

as it is done with the Kaimal spectrum in the Danish code of practice for wind turbines DS 412 [24]. More realistic, terrain dependent length scales for the turbulence in heights above 30 m can be obtained from the Eurocode [25].

If the spectral distribution is a Kaimal spectrum, the friction velocity u_* can simply be determined by

$$u_*^2 = 0.21\sigma^2 = 0.21(I \cdot V_0)^2 \tag{38}$$

where σ is the standard deviation of the wind speed and $I=\sigma/V_0$ is the turbulence intensity.

The two-sided Højstrup spectrum $S_{Hoj}(f)$ [26] can be written as

$$S_{Hoj}(f) = u_*^2 \left(\frac{2.4\,\frac{L}{V_0}}{\left(1 + 1.5\,\frac{L}{V_0} f\right)^{5/3}} + \frac{2.5\,\frac{A_{Hoj}}{V_0}}{1 + 2.2\left(\frac{A_{Hoj}}{V_0} f\right)^{5/3}} \right) \cdot \frac{1}{1 + 0.94\left(\frac{L}{A_{Hoj}}\right)^{2/3}} \tag{39}$$

The Højstrup spectrum introduces an additional length scale A_{Hoj}, which Højstrup determined experimentally to A_{Hoj}=3000m.

5.2.4 Coherence

As it is seen from section 5.2.2, it is straight forward to use any coherence function with the PARKWIND method. We have chosen to implement a Davenport [26] type coherence, and use the decay factors recommended by Schlez and Infield [28] as default values in the program. Schlez and Infield studied the horizontal two-point coherence for separations greater than the measurement height, and their recommendations are based on estimates on own measurements and several other measurements.

The Davenport type coherence function between the two points r and c (see Figure 22) can be defined in the square root form

$$\gamma(f, d_{rc}, V_0) = e^{-a_{rc}\frac{d_{rc}}{V_0} f} \tag{40}$$

where a_{rc} is the decay factor. Schlez and Infield uses a decay factor which depends on the inflow angle α_{rc} shown in Figure 22. The figure shows that α_{rc}=0 corresponds to longitudinal flow, and α_{rc}=90deg corresponds to lateral flow.

With a given α_{rc}, the decay factor can be expressed according to

$$a_{rc} = \sqrt{(a_{long}\cos\alpha_{rc})^2 + (a_{lat}\sin\alpha_{rc})^2} \tag{41}$$

where a_{long} and a_{lat} are the decay factors for longitudinal and lateral flow respectively. Using our definition of coherence decay factors in (40) (41), the recommendation of Schlez and Infields can be rewritten as to use the decay factors

$$a_{long} = (15 \pm 5) \cdot \frac{\sigma}{V_0} \tag{42}$$

$$a_{lat} = (17.5 \pm 5) \cdot \sigma \tag{43}$$

using the standard deviation of the wind speed σ in m/s.

5.3 Rotor wind model

5.3.1 Equivalent wind speed

As described in section 5.1, the rotor wind model provides an equivalent wind speed v_{eq}, which takes into account the variations due to turbulence and tower shadow in the wind speed field over the rotor disk. This section describes how the equivalent wind speed is derived from the rotor wind speed field.

Figure 23 shows the three bladed wind turbine with the wind field $v(t,r,\theta)$. It is seen that the positions are given in the polar coordinates (r,θ), where θ denotes the azimuth angle.

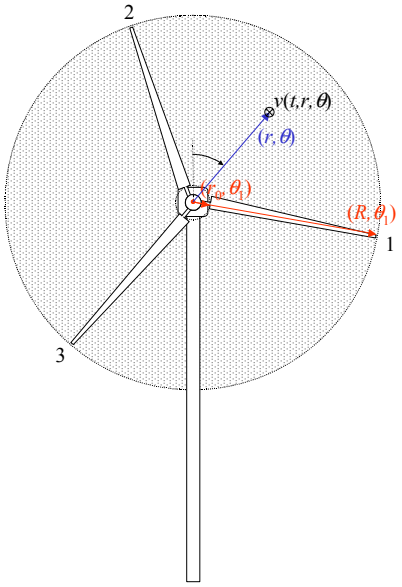

Figure 23. The wind speed field in the rotor plane is given as $v(t,r,\theta)$, the blade aerodynamic profile extends from the inner radius r_0 to the outer Radius R. The figure also indicates azimuth position θ_1 of blade number 1.

The aerodynamic torque $T_{ae}(t)$ is given as the sum of the blade root moments $M_b(t)$ in the drive direction of each blade b, i.e.

$$T_{ae}(t) = \sum_{b=1}^{3} M_b(t) \tag{44}$$

Figure 23 indicates that the blade aerodynamic profile extends from the inner radius r_0 to the outer radius R of the rotor disk. Linearising the blade root moment dependence on the wind speed we obtain

$$M_b(t) = M(V_0) + \int_{r_0}^{R} \psi(r)\left(v(t, r, \theta_b) - V_0\right)dr \tag{45}$$

where $M(v_0)$ is the steady state blade root moment corresponding to the mean wind speed V_0, and $\psi(r)$ is the influence coefficient of the aero load on the blade root moment in radius r.

For aero torque, a typical load distribution along the blades can be obtained by assuming $\psi(r)$ to be proportional to r and r_0=0.1R, which has also been assumed in the implemented model. However, for the sake of completeness, we will formally keep $\psi(r)$ and r_0 here.

Inserting (45) in (44) we obtain

$$T_{ae}(t) = 3M(V_0) + \sum_{b=1}^{3} \int_{r_0}^{R} \psi(r)\left(v(t, r, \theta_b) - V_0\right)dr \tag{46}$$

Now we define the equivalent wind speed $v_{eq}(t)$ as the wind speed which is independent on the position in the rotor disk, and would give the same aerodynamic torque as the actual wind speed field, i.e. $v_{eq}(t)$ must fulfil

$$T_{ae}(t) = 3M(V_0) + \sum_{b=1}^{3} \int_{r_0}^{R} \psi(r)\left(v_{eq}(t) - V_0\right)dr \tag{47}$$

Combining (47) with (46) gives the equivalent wind speed as the mean value of contributions from all three blades:

$$v_{eq}(t) = \frac{1}{3}\sum_{b=1}^{3} v_{\psi}(t,\theta_b) \tag{48}$$

where we have used the weighted wind speed $v_{\psi}(t,\theta_b)$ defined as

$$v_{\psi}(t,\theta_b) = \frac{\int_{r_0}^{R} \psi(r) v(t,r,\theta_b) dr}{\int_{r_0}^{R} \psi(r) dr} \tag{49}$$

(48) and (49) express the equivalent wind speed as a weighting of all the wind speeds which are instantaneously seen by the wind turbines along the blades. We could now simulate the wind speeds in a number of points in the rotor plane as typically done in codes for simulation of mechanical loads on wind turbines. However, a much more computer time saving simulation method for simulation of the equivalent wind speed has been developed in Risø National Laboratory.

This simulation method was first presented by Langreder [29] for the contribution from turbulence, and compared the model to simulations with a cross power spectral method. Later, Rosas et.al. [17] verified the model against measurements, and included tower shadow effects in the method. In this paper, it is combined with the park scale model.

The equivalent wind speed simulation method is based on Risøs frequency domain models, Madsen and Rasmussens [30] and Sørensen et.al. [31][32]. These frequency domain models are based on expansion of the wind speed field in the rotor plane in the azimuth angle.

To understand the simulation model, we first expand the weighted wind speed for a single blade in the azimuth angle, i.e.

$$v_{\psi}(t,\theta_b) = \sum_{k=-\infty}^{\infty} \tilde{v}_{\psi,k}(t) e^{jk\theta_b} \tag{50}$$

where $\tilde{v}_{\psi,k}(t)$ is the k^{th} azimuth expansion coefficient of $v(t,\theta_b)$ determined according to

$$\tilde{v}_{\psi,k}(t) = \frac{1}{2\pi}\int_0^{2\pi} v_{\psi}(t,\theta_b) e^{-jn\theta} d\theta \tag{51}$$

Inserting (50) in (48) yields

$$v_{eq}(t) = \sum_{k=-\infty}^{\infty} \tilde{v}_{\psi,3k}(t) e^{j3k\theta_{WTR}} \tag{52}$$

where $\theta_{WTR}=\theta_1$ is the wind turbine rotor position obtained from the mechanical model.

It is seen from (52) that only the azimuth expansion coefficients with orders which are multiple of 3 contribute to the sum. This is because of the symmetric structure of rotor, which causes the contributions from the other orders to sum up to zero for all three blades. If a 1p and/or 2p variation is still significant in a measurement of torque or power, this is often an indication that the blades are not pitched with exactly the same angle.

In the present implementation in DIgSILENT, we have only included the 0^{th} and 3^{rd} harmonics, i.e. (52) has been approximated to

$$v_{eq}(t) \approx \tilde{v}_{\psi,0}(t) + 2\,\mathrm{Re}\{\tilde{v}_{\psi,3}(t)\}\cos(3\theta_{WTR}) + 2\,\mathrm{Im}\{\tilde{v}_{\psi,3}(t)\}\sin(3\theta_{WTR}) \tag{53}$$

The idea of the rotor wind model is to simulate the azimuth expansion coefficients $\tilde{v}_{\psi,k}(t)$ in the first place as independent on the azimuth position of the rotor, and then use (53) to generate the equivalent wind speed which includes the azimuth dependence.

The azimuth expansion coefficients $\tilde{v}_{\psi,k}(t)$ are sums of contributions from the turbulence model, tower model and the mean wind speed. The mean wind speed contributes with V_0 to $\tilde{v}_{\psi,0}(t)$. The contributions from the turbulence model and the tower model are determined in the next subsections.

Other effects like wind shear and yaw error could have been included, but these effects mainly contribute to the 1p, which is filtered away by the summation of the 3 symmetric blades.

5.3.2 Turbulence model

As a consequence of the description above, the turbulence model generates the azimuth expansion coefficients $\tilde{v}_{\psi,k,turb}(t)$ of the turbulence field. It has been shown [30],[32] the power spectral density (PSD) $S_{\tilde{v}_{\psi,k}}(f)$ of $\tilde{v}_{\psi,k,turb}(t)$ can be determined according to

$$S_{\tilde{v}_{\psi,k}}(f) = F_{\tilde{v}_{\psi,k}}(f) \cdot S_v(f) \tag{54}$$

$S_v(f)$ is the PSD of the wind speed in a fixed point, and $F_{\tilde{v}_{\psi,k}}(f)$ is an admittance function. $F_{\tilde{v}_{\psi,k}}(f)$ can be determined by a triple integral, which can be resolved into the double integral

$$F_{\tilde{v}_{\psi,k}}(f) = \frac{\int_{r_0}^{R}\int_{r_0}^{R} \psi(r_1)\psi(r_2)F_k(f, r_1, r_2)dr_1dr_2}{\left(\int_{r_0}^{R}\psi(r)dr\right)^2} \tag{55}$$

with an inner single integral

$$F_k(f, r_1, r_2) = \frac{1}{2\pi}\int_0^{2\pi} \gamma_{lv}\left(f, \sqrt{r_1^2 + r_2^2 - 2r_1r_2\cos(\theta)}\right)\cos(n\theta)d\theta \tag{56}$$

Here, $\gamma_{lv}(f,d)$ is the square root coherence function between two points with a distance d in the rotor plane. $\gamma_{lv}(f,d)$ is assumed to be the same horizontally (i.e. laterally) and vertically in the plane.

(55) and (56) have been solved numerically by Sørensen [32]. Using the Laplace operator $s=j\omega= j2\pi f$, Langreder [29] defined the transfer functions $H_{\tilde{v}_{\psi,k}}(j2\pi f)$ with the size defined as

$$\left|H_{\psi,k}(j2\pi f)\right| = \sqrt{F_{\tilde{v}_{\psi,k}}(f)} \tag{57}$$

and used the numerical results to fit $H_{\tilde{v}_{\psi,0}}(j2\pi f)$ and $H_{\tilde{v}_{\psi,3}}(j2\pi f)$ to linear filters. Defining the constant $d=R/V_0$, the results of these fittings are

$$H_{\psi,0}(s) \approx \frac{0.99 + 4.79ds}{1 + 7.35ds + 7.68(ds)^2} \tag{58}$$

$$H_{\psi,3}(s) \approx \frac{0.0307 + 0.277ds}{1 + 1.77ds + 0.369(ds)^2} \tag{59}$$

Using $v_{hub}(t)$ from the park scale model as input and a linear filter with the transfer function $H_{\psi,0}(j2\pi f)$, $\widetilde{v}_{\psi,0,turb}(t)$ is now simulated according to

$$\widetilde{V}_{\psi,0,turb}(f) = H_{\psi,0}(j2\pi f) \cdot V_{hub}(f) \tag{60}$$

where $\widetilde{V}_{\psi,0,turb}(f)$ and $V_{hub}(f)$ are the Fourier transforms of $\widetilde{v}_{\psi,0,turb}(t)$ and $v_{hub}(t)$ respectively.

(60) introduces an unintended phase shift in $\widetilde{v}_{\psi,0,turb}(t)$ and $v_{hub}(t)$. However, the phase shift is the same for all wind turbines in the park, assuming the same $d=R/V_0$, i.e. mean wind speed and rotor disk radius. The relatively small changes of mean wind speed in the park have only little influence on this.

$\widetilde{v}_{\psi,3,turb}(t)$ is a complex variable, and it has been shown that the real and imaginary parts are uncorrelated with each other and with azimuth expansion coefficients of other orders k. Distributing the variance between the real and imaginary parts of $\widetilde{v}_{\psi,3,turb}(t)$ evenly, they are determined by the relations between Fourier transforms

$$\mathrm{Re}\left\{\widetilde{V}_{\psi,3,turb}(f)\right\} = \frac{1}{\sqrt{2}} H_{\psi,3}(j2\pi f) \cdot V_{3,\mathrm{Re}}(f) \tag{61}$$

$$\mathrm{Im}\left\{\widetilde{V}_{\psi,3,turb}(f)\right\} = \frac{1}{\sqrt{2}} H_{\psi,3}(j2\pi f) \cdot V_{3,\mathrm{Im}}(f) \tag{62}$$

where $V_{3,\mathrm{Re}}(f)$ and $V_{3,\mathrm{Im}}(f)$ are Fourier transforms of uncorrelated stochastic signals with the same PSD as the wind speed in a fixed point.

To support the simulation of $V_{3,\mathrm{Re}}(f)$ and $V_{3,\mathrm{Im}}(f)$, Langreder also fitted a filter which converts uniformly distributed white noise to a signal with the PSD as the Kaimal spectrum.

5.3.3 Tower shadow model

Today most wind turbines are constructed with a rotor upwind of the tower to reduce the tower interference of the wind flow. Early wind turbines often had lattice towers, but for visual reasons, tubular towers are the most common today.

The tubular towers have some effect on the flow. In the upwind rotor case, the tower disturbance v_{tow} can be modelled using potential flow theory. Ekelund [33] found

$$v_{tow} = V_0 a^2 \frac{x^2 - y^2}{\left(x^2 + y^2\right)^2} \tag{63}$$

where V_0 is the mean wind speed, a is the tower radius, and x and y are the components of the distance from each blade to the tower centre in the lateral and the longitudinal directions, respectively.

Rosas used (63), (49) and (51) to calculate the azimuth expansion coefficients caused by the tower shadow. Neglecting the effect of the blade bending, these coefficients become constants $\widetilde{v}_{\psi,k,tow}$, which can be added to contributions from the turbulence.

6 Verification of PARKWIND model

The parkscale wind model, which is implemented in the PARKWIND program code, has been verified using wind speed measurements on two masts SMW and SMS on the Vindeby offshore site. The distance between the two masts was 807 m.

Figure 24 shows one hour of one minute mean values of measurements of the mean wind speeds around 11 m/s and wind directions which provides an almost longitudinal separation of the flow from SMW to SMS. The figure also shows PARKWIND simulations with the same mean wind speed and wind direction.

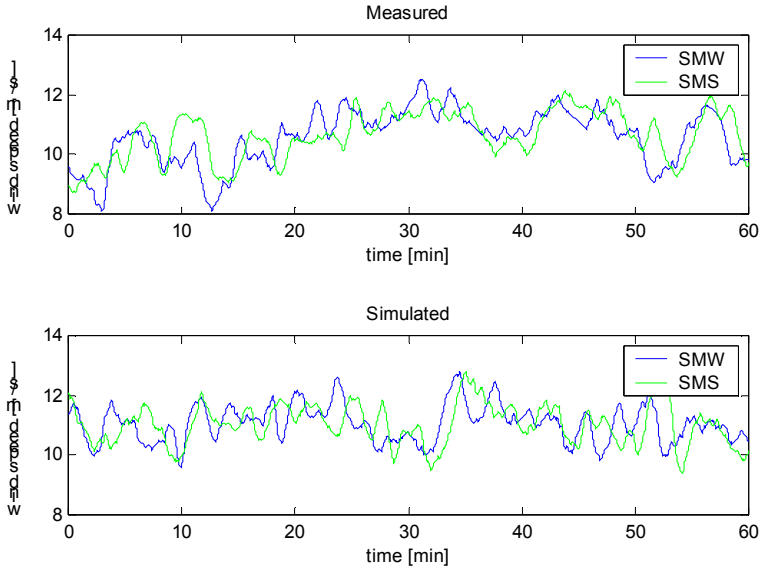

Figure 24: Simulation of wind speeds compared to measurements on two sea masts in Vindeby offshore wind farm.

Both measurements and PARKWIND indicate a delay of SMS with a little more than one minute relative to SMW. This corresponds very well to the expected delay for 11 m/s with 807 m distance.

A more reliable verification is to compare the coherence functions. However, this requires a substantial data set, because the coherence in 807 m distance is fairly small, especially for wind directions with lateral separation between the two masts.

Figure 25 shows the square root coherence of 6×6 hours wind speed with almost longitudinal separation.

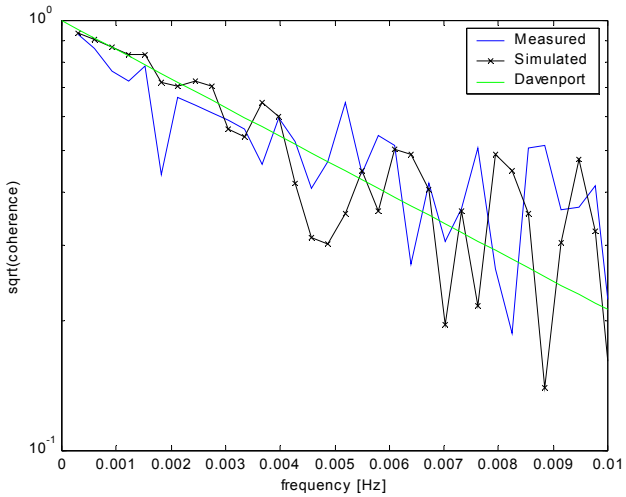

Figure 25: Square root coherence function of measured and simulated 6×6 hours wind speed time series on Vindeby SMW and SMS.

The inflow angle of the measurements has been calculated from the mean value of the wind direction in each time series, and used to determine the decay factor for the coherence according to (41) for the simulations. The Davenport coherence is also indicated in the figure as a straight line.

7 Verification of DIgSILENT model

7.1 Measurements

Two campaigns of simultaneous measurements on Hagesholm have been used for the verification of the model. The first campaign is NEG-Micons power curve and mechanical load measurements done by WINDTEST. The second campaign is a power quality test performed by Risø dedicated the verification of the electric part of the model. The WINDTEST and Risø measurements have been performed simultaneously, but not synchronised. However, the power of wind turbine 1 was measured in both campaigns, and this has been used to post synchronise the measurements.

The WINDTEST measurements are performed with 25 Hz sampling frequency. They comprise the signals required for power curve measurements on both wind turbine 1 and wind turbine 2, and a comprehensive load test of wind turbine 1, comprising blade, shaft and tower loads. The wind speed was measured in hub height on a mast west to turbine 1. The WINDTEST data is stored in files with 10 minute time series, with continuous measurements from the end of one file to the beginning of the next file.

The Risø measurements are power quality tests on wind turbine 1, performed according to IEC 61400-21. The power quality measurements comprise instantaneous values of 3 phase voltages and currents logged together with the wind speed. The cup anemometer of the control system on the nacelle was used for

the wind speed measurements. The sampling frequency of the power quality test was 3.2 kHz for all channels. Data is stored in files with time series of 700 s period length, which ensures 10 minutes of continuous data plus time for initialisation of filters in the power quality analysis software. The data logging is interrupted approximately 4 minutes after each 700 s run, to allocate computer time for the power quality calculations between the runs.

Eight Risø runs have been selected for the verification, six with mean wind speeds around 9 m/s and two with mean wind speeds around 15 m/s. The wind direction was SW, which ensures that neither wind turbine 1 nor wind turbine 2 are in wake of other wind turbines. The main statistical data for each time series are shown in Table 3 (Appendix A).

In this chapter, we will use one typical run at 9 m/s to demonstrate the verification of the simulations and one at 15 m/s, but all 8 runs are used for the verification. Therefore, tables and graphs for all 8 runs are shown in Appendix A.

The eight Risø runs were synchronised with the WINDTEST measurements by estimating the cross correlation function $R_{RW}(\tau)$ between Risøs and WINDTESTs measurements of power on wind turbine 1. The value of τ for which $R_{RW}(\tau)$ is maximum has been used to determine the exact time delay for each 700 s run of Risø measurements relative to the continuous WINDTEST measurements.

For comparison to the simulations which provides RMS values, and for the power quality assessments, Risøs software has been used to calculate power quality measures from the instantaneous values of voltages and currents. The software comprises fits of amplitudes and phases of voltage and current fundamentals, calculation of active and reactive power and flicker calculations.

7.2 Simulations

The simulations were carried out in two steps, first by simulating the hub wind speeds with PARKWIND, and then using these hub wind speeds as input to DIgSILENT simulations. Eight simulations were performed with input data corresponding to the eight selected measurement runs. For each run, the statistics of WINDTESTs wind speed and power measurements have been used to estimate the input parameters for the wind model.

The power spectral density of the wind speed has been estimated based on WINDTESTs wind speed measurements. The spectra have been assumed to be of the Kaimal type (36) with length scales L=600 m according to (37). u_* in (36) has been estimated by the mean wind speed V_0 and turbulence intensity I according to (38).

Figure 26 shows the PSD of the measured wind speed together with the fitted Kaimal spectrum for the typical 9 m/s run. It is seen that the Kaimal spectrum is a good assumption in this case, and for the other seven runs, Figure 45 (Appendix A) shows that the Kaimal spectrum fits good. The sudden drop of the PSD of the measured wind speeds around 0.5 Hz is due to the filtering in the measurement procedure for determination of the anemometer pulse frequency. Thus the difference between measurement and fit at frequencies above 5 Hz is mainly explained by the measurement procedure, which is optimised for mean wind speed determination rather than determination of wind speed fluctuations.

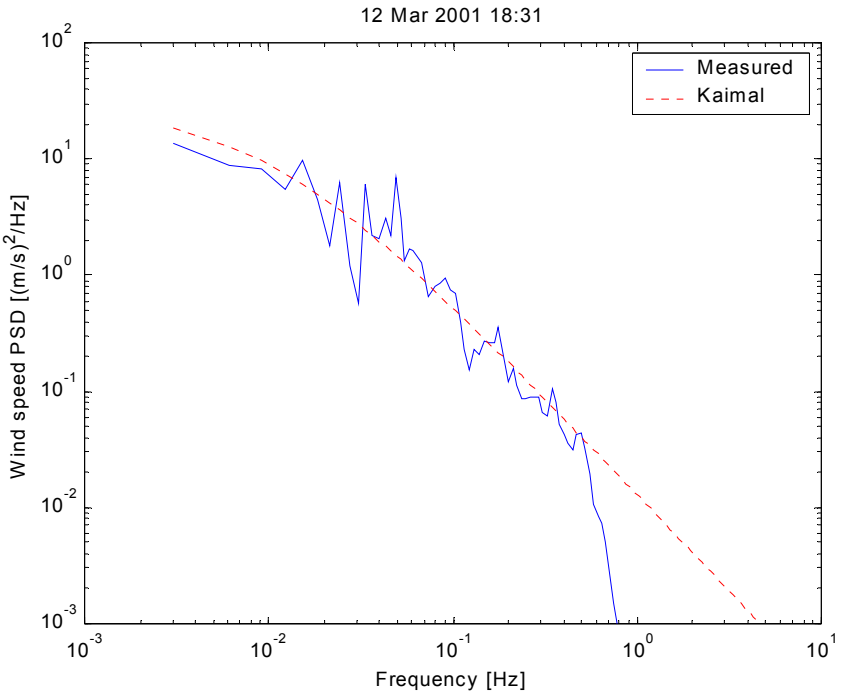

Figure 26. Measured and (Kaimal) fitted power spectral density of wind speed of the typical 9 m/s run.

With the intention to ensure that the mean value of the power at the wind turbines is the same in the simulations as in the measurements, a power curve for the wind turbine has been simulated, and used to adjust the mean wind speeds used in the simulations. This adjustment is intended to make comparisons of measured and simulated maximum power more realistic, referring to the same mean values of power.

The simulated power curve is shown in Figure 27. It is seen that the adjustment of the wind speed only makes sense for the first six runs at approximately 9 m/s mean wind speed, because the power curve is flat at 15 m/s, and therefore the measured power cannot be used to estimate the wind speed in that area.

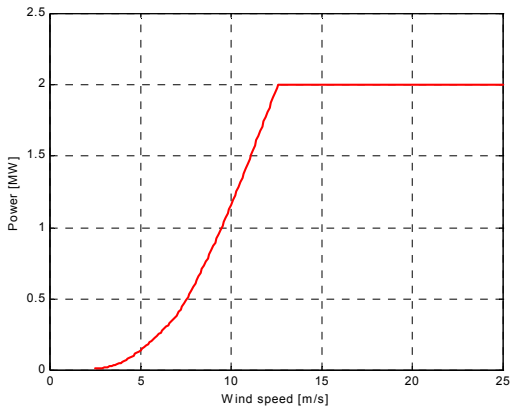

Figure 27. Simulated power curve used to fit the wind speeds for the simulations.

Still, the adjusted wind speeds do not result in exactly the same mean values of simulated power as of measured power. Among other reasons, this is because the adjustment of the mean wind speed was based only on the power measured on wind turbine 1. PARKWIND assumes the mean wind speed to be the same for all the wind turbines. Another reason is that the time series simulated with

PARKWIND in the first place were longer than 600 s, while the compared time series are windows of 600 s length, where the mean wind speeds are not exactly the same as for the whole simulation period. The statistics of the simulated wind speed and power is shown in brackets in Table 3 (Appendix A).

7.3 Power fluctuations and mechanical loads

The power fluctuations from a wind farm are relevant because they contribute to the flicker emission from the wind farm and the maximum power from the wind farm. In some cases, the power fluctuations can also influence the power system control. In this section, we will compare the fluctuations of the simulated power to the fluctuations of the measured power for continuous operation of the wind turbines, to get an overview of at which frequencies the present model can predict the power fluctuations.

Figure 28 shows the PSD of 10 minutes measured and simulated power for the typical 9 m/s run. It is seen that the frequencies below 1 Hz are predicted quite well, whereas the measurements reveal fluctuations above 1 Hz which are not included in the model. Also a 1p at 0.3 Hz is seen in the measurements, but not in the simulations.

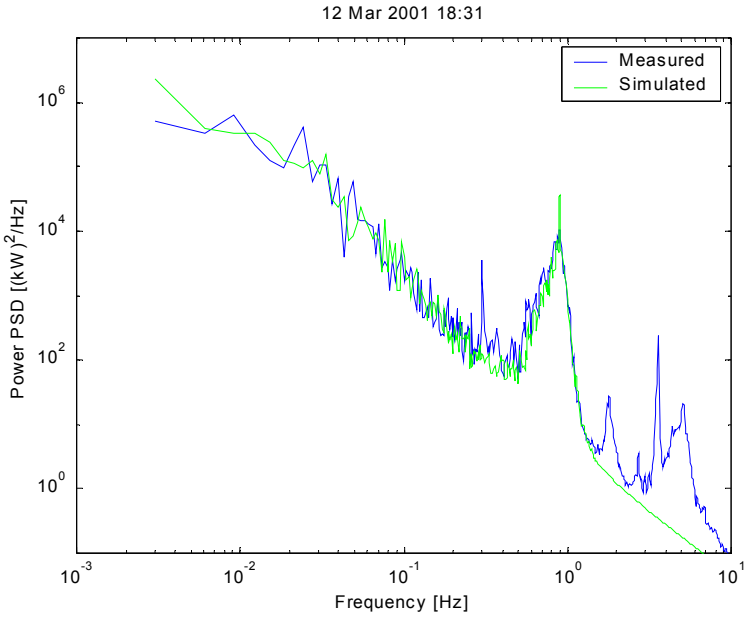

Figure 28. PSD of measured and simulated power fluctuations of wind turbine 1 at approximately 9 m/s.

The simulated torques have also been compared to the measured. The results for the same run as in Figure 28 are shown in Figure 29. Both the simulated aerodynamic torque T_{ae} and the simulated low speed shaft torque T_{lss} (see Figure 17) are shown together with the measured torque, which corresponds to T_{lss}. It is seen in Figure 29 how the flexibility of the shaft adds energy to the PSD of T_{lss} relative to T_{ae} at the eigenfrequency 0.7 Hz, and thereby the PSD of T_{lss} comes close to the PSD of the measured torque. This indicates that the mechanical model predicts the shaft flexibility quite well.

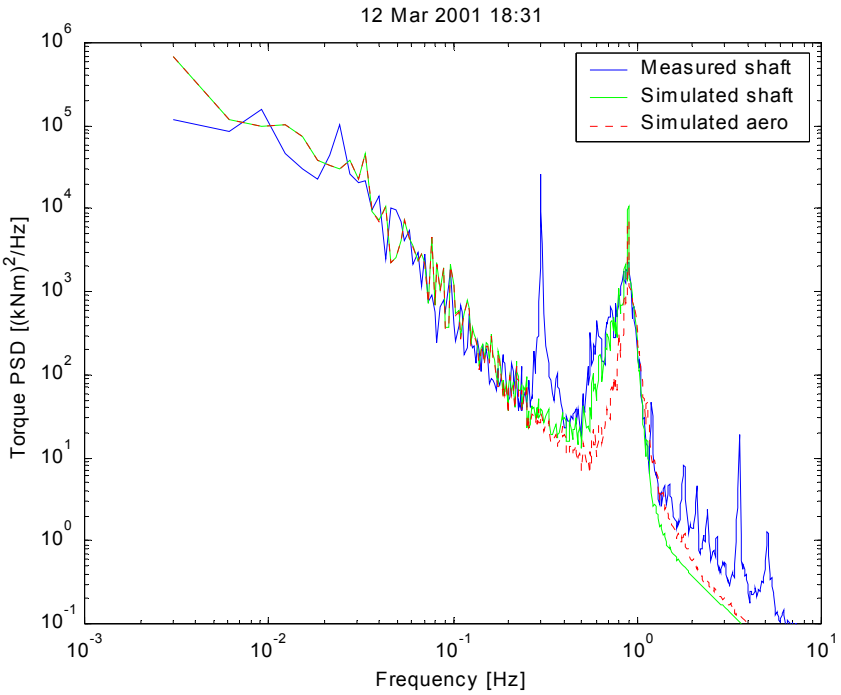

Figure 29. PSD of measured and simulated torque fluctuations of wind turbine 1 at means wind speed 9 m/s.

A remarkable frequency in Figure 29 is the 1*p* frequency of the measured torque. The maximum at 1*p* is relatively higher than the maximum at 3*p*. Part of this is due to some unsymmetry in the rotor, which is also reflected in the power. However, there is no good reason why the gearbox or generator should filter the 1*p* harder than the 3*p*. As torque measurements with strain gauges are quite sensitive to cross-talking, it is therefore assumed that most of the 1*p* in the torque is due to such cross-talking.

In the PSDs of the power as well as the torques, "spikes" are visible exactly at the 3*p* frequencies for the simulations. This is due to the tower shadow model. The corresponding spikes in the measured PSDs are significantly smaller.

Apart from the 3*p* frequency 0.9 Hz and the drive train eigenfrequency 0.7 Hz, the 6*p* and particularly the 12*p* frequencies are evident from the power PSDs. These frequencies can easily be included in the model, although it is not clear why the 12*p* is as distinct as it is compared to 9*p* and even 6*p*. With the applied model for tower shadow and turbulence, it should be expected that the *p*'s decrease in size when they increase in order.

Finally, a frequency around 5 Hz is evident from the PSDs of measured power and torque. This frequency is not included in the simulation. The 5 Hz frequency can also be seen in the bending moments on the main shaft and tower, e.g. in the tilting moment of the shaft as shown in Figure 30. It is therefore assumed that the 5 Hz frequency must be a mechanical eigenfrequency, but it is not clear which mode it is.

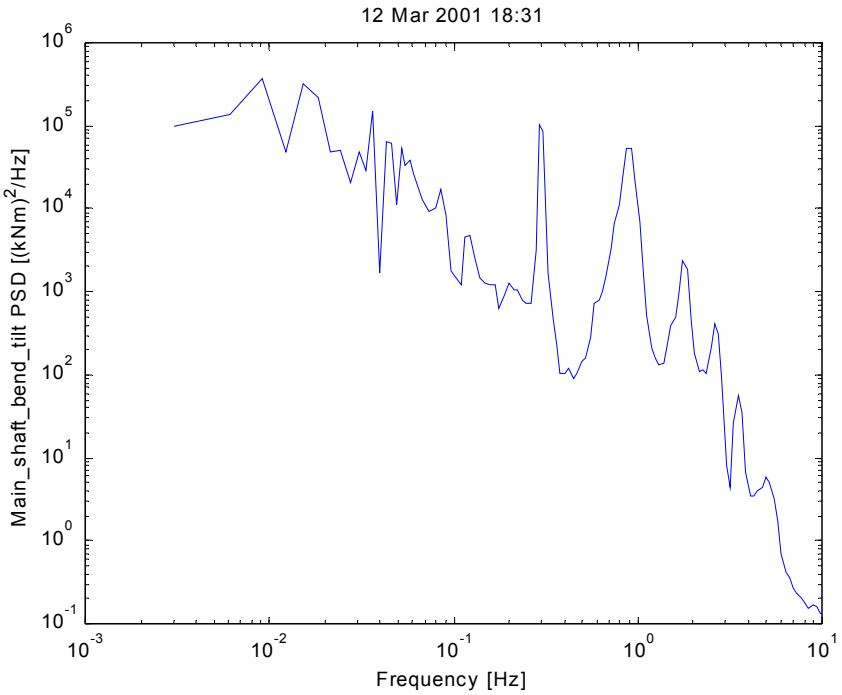

Figure 30. PSD of measured main shaft tilt on wind turbine 1 at mean wind speed 9 m/s.

The PSDs of measured and simulated power at approximately 14 m/s are shown in Figure 31. To illustrate the effect of a dynamic stall model described in section 4.4, the simulations are performed with and with a steady state aerodynamic model as well as the dynamic stall model. At the first view, the simulation with dynamic stall model seems to be as good as the simulations with wind speeds about 9 m/s. Also the PSD of the simulation without dynamic stall model looks acceptable, though it is clear from Figure 31 that the dynamic stall model improves the simulations.

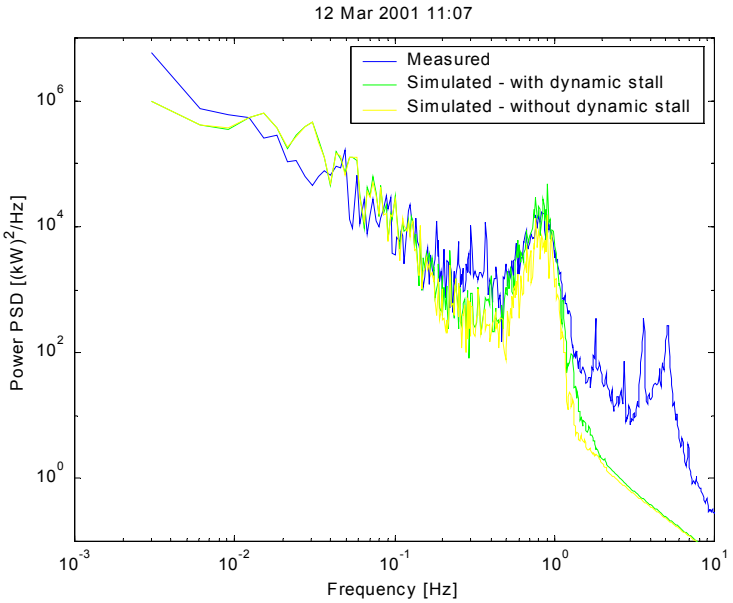

Figure 31. PSD of measured and simulated power fluctuations of wind turbine 1 at approximately 14 m/s.

However, if we look at the time series in Figure 32, we get a more detailed impression. To compare the time series, one must know that the measurements and simulations are done with different wind speed time series, so that the time series cannot be compared from step to step. Still, the character of the fluctuations can be compared. Also, the two simulations are done with identical wind speed input, which can also be seen from Figure 32.

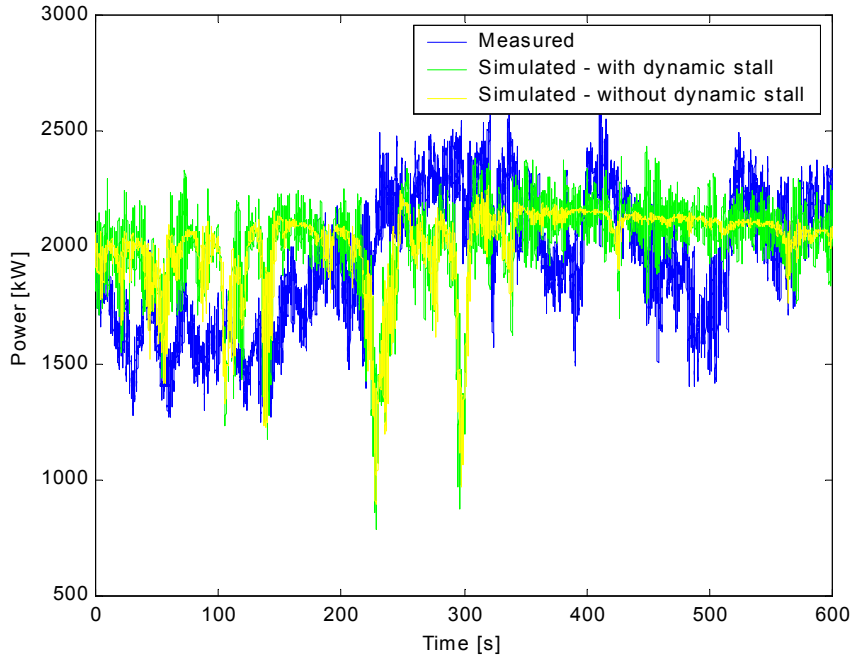

Figure 32. Time series of measured and simulated power fluctuations of wind turbine 1 at approximately 14 m/s.

The character of the first 300 seconds of the simulations are in good agreement to the measurements, while the last 300 seconds of simulations are significantly different from the measurements. In the last 300 seconds, the simulations have very little slow fluctuations, and the fast (3p) fluctuations are strongly reduced without dynamic stall model. This is because the wind speed increases, and the simulation goes into deep stall.

Consequently, from the last 300 seconds we observe two things: The first is that the dynamic stall model is very important to simulate the fast fluctuations in deep stall, while the second is that the slow fluctuations are not simulated well enough.

One reason why the slow fluctuations are not simulated well enough can be that the model only includes the longitudinal component of the wind speed. The transverse wind speed component are more important for high wind speeds than for low wind speeds, obviously because the fluctuations are larger for higher wind speeds, but mainly because the $C_p(\lambda)$ curve is very steep in that region. Studies of the slope of the $C_p(\lambda)$ curve in the stall region have shown that a transversal wind speed of 1 m/s will increase C_p with 5 % corresponding to 100 kW.

A transversal component of the wind speed can be included in the model as a modification of λ in (15), which adds an equivalent transversal wind speed component x_{eq} to the tip wind speed, i.e.

$$\lambda = \frac{\omega_{WTR} \cdot R + x_{eq}}{u_{eq}} \tag{64}$$

The idea in (64) is that λ is actually not the tip speed ratio, but the ratio between the two perpendicular relative wind speed components seen from sections of a rotating blade. λ determines the angle of attack, which together with longitudinal equivalent wind speed u_{eq} determines the aerodynamic power according to (16). Aerodynamic models where only the longitudinal component of the wind speed is considered, are actually a specific case, where λ becomes the tip speed ratio.

Another reason why the slow fluctuations are not simulated well enough can be the uncertainty in the aerodynamic data. Finally, the modelling of the active stall control has been difficult, because the algorithm is fairly complicated and because the wind turbine in Hagesholm has been used by NEG-Micon to make experiments with and development of the active stall control when the wind speed was high.

7.4 Reactive power fluctuations

The reactive power measured on the 10 kV terminal of the wind turbine follows the fluctuations in the active power because of the leakage reactances in the induction generator as well as the transformer. As described in section 4.2.1, the wind turbine is full load compensated by a capacitor bank with steps of 50 kvar, and to avoid unnecessary wear of the electric components, the capacitors are only switched after some averaging period.

The dynamic behaviour of the reactive power consumption relative to the fluctuations in active power are shown in Figure 33 for the typical 9 m/s case. It is seen that the simulated and measured values group on two curves each, corresponding to two different numbers of capacitors switched on.

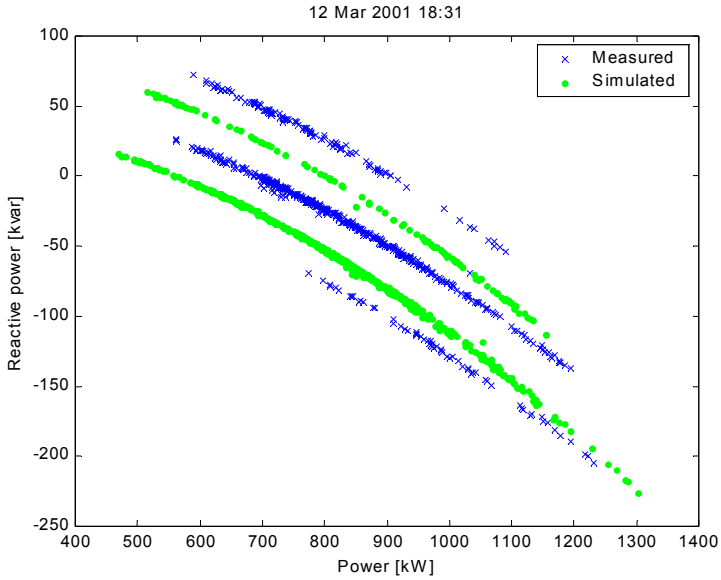

Figure 33. Measured and simulated 1 second average values of reactive power vs. active power for 10 minutes data in the typical 9 m/s run.

The simulated PQ-curves are almost parallel displacements of the measured curves, but they do not have the same level. This effect could be caused by different voltages for simulations and measurements, but the tap regulation in the substation transformers have been set so that the voltage is the same in simulations and measurements. A better explanation for the difference is that the rated values of the capacitors have been used in the simulations, whereas the real ca-

pacitors have some tolerance. The standard tolerances of the capacitors can be -5 % to +15 % for units up to 100 kvar according to IEC 831-1 [34].

We could have measured and modelled each individual capacitor to have a more accurate simulation. However, such a detailing of the model would not be of much use, because the closed loop regulation of the capacitor switches ensures that the average values of the simulations are close to the measured average values, which can also be seen from the results in section 8.3.

Taking the tolerance into account, the simulated curves should be parallel displacements of the measured curves. The small difference in that respect is probably because of the leakage reactances, which also deviate slightly from the modelled values. As the comparisons of the PQ-curves are done on the 10 kV terminals of the wind turbine, the leakage reactances of the step-up transformers as well as the induction generators influence the slope of the PQ-curves.

7.5 Summation of power fluctuations

The simultaneous power measurements on wind turbine 1 and wind turbine 2 have been used to verify the prediction of summed power from two wind turbines. The cross correlation coefficients between the power from the two wind turbines are used to compare measurements to simulations.

The advantage of comparing correlation coefficients is that the correlation coefficients ρ provide a simple relation between the standard deviations σ_{P1} and σ_{P2} of the two power time series p_1 and p_2, and the standard deviation σ_{P1+P2} of the sum of these time series, namely

$$\sigma_{P_1+P_2} = \sqrt{\sigma_{P_1}^2 + \sigma_{P_2}^2 + 2\rho\sigma_{P_1}\sigma_{P_2}} \tag{65}$$

With N identical wind turbines with the same power standard deviation σ_P, the standard deviation of the sum of the powers, $\sigma_{\Sigma P} = \sqrt{N}\,\sigma_P$ if the power time series of the wind turbines were uncorrelated ($\rho = 0$) and $\sigma_{\Sigma P} = N\sigma_P$ if the power time series were identical ($\rho = 1$). For the power of wind turbines in a wind farm, the standard deviation of the sum is normally between these two extremes, i.e. $\sqrt{N}\,\sigma_P < \sigma_{\Sigma P} < N\sigma_P$ corresponding to correlation coefficients $0 < \rho < 1$.

The results of measured and simulated correlation coefficients are shown in Figure 34. First of all it is observed that there is a large scatter between the results of both measured and simulated correlation coefficients, especially for the six runs at approximately 9 m/s. This is because the statistical uncertainty of the correlation coefficients are high.

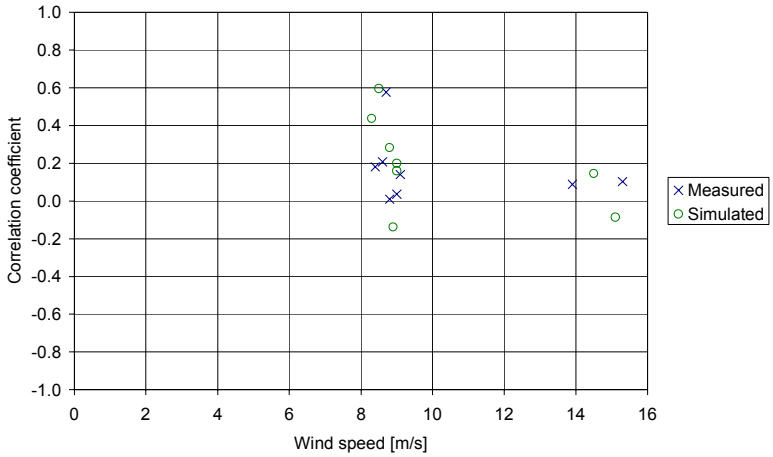

Figure 34. Correlation coefficients between power at wind turbine 1 and wind turbine 2 for measured and simulated power.

The next thing which is observed in Figure 34 is that a significant majority of both measured and simulated correlation coefficients are positive, which confirms that the power fluctuations of wind turbine 1 and wind turbine 2 are actually correlated. The correlation seems to be stronger at 9 m/s than at 15 m/s, which is because the slow fluctuations are much more correlated than the fast fluctuations, and there are more slow fluctuations in the linear region about 9 m/s than in the stall region about 15 m/s. However, a statistical basis of two 10 minute time series is very little to assess the correlation coefficients at 15 m/s.

Finally, the 95 % confidence interval of the six measured correlation coefficients at 9 m/s have been estimated to 0.19±0.16, while the simulated correlation coefficient are 0.26±0.20. This underlines the conclusion that the measured power fluctuations are correlated, and that the estimated mean value of the simulated correlation coefficients are within the confidence interval of the measured correlation coefficients. However, the statistical analyses must be based on a much higher number of runs to assess the difference between simulations and measurements.

7.6 Voltage fluctuations

As already mentioned, the voltage was measured on the 10 kV terminals of wind turbine 1. At that point, the wind farm contribution to the voltage fluctuations is expected to be quite dominating. However, other sources in the grid also contribute to the voltage fluctuations. In the present simulation model, only the fluctuations caused by the wind farm are included.

This is illustrated in Figure 35, where the PSDs of measured and simulated voltages are shown. It is seen that the simulation predicts the frequencies around the 3*p* (0.9 Hz) very well, because the wind farm provides the main contribution at these frequencies. But it is also seen that there is additional noise on the grid voltage distributed over the whole frequency range.

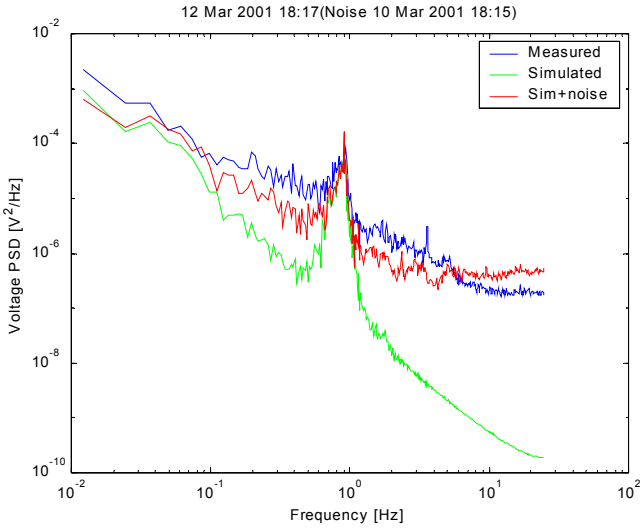

Figure 35. PSDs of measured (positive sequence) voltage and simulated voltage on the 10 kV terminal of wind turbine 1in the typical 9 m/s run.

This noise is probably not caused by the wind farm. This is a reasonable assumption because the gap between simulated and measured voltage in much higher than between simulated and measured power. It is also confirmed by voltage measurements when the wind speed is below cut-in wind speed, which provides the background noise to the voltage, caused by other sources than the wind farm. We have found voltage measurements with low wind speeds two days before the 9 m/s measurements, and confirmed that no wind turbines were connected because no 3*p* frequency could be observed on the voltage. Assuming that the background voltage noise is not correlated with the wind farm fluctuations, the PSD of the voltage on the no-wind day has been added to the simulated PSD to illustrate what could be the PSD of the simulated voltage if a similar background noise in modelled. There is still some difference between simulated + noise voltage on one side, and measured voltage on the other side. This could be because there is more background noise, e.g. because other wind turbines also contribute to the voltage fluctuations.

8 IEC 61400-21 characteristics

8.1 General

IEC 61400-21 specifies methods to measure and assess the power quality of grid connected wind turbines. The measurement methods include specification of the measurement hardware as well as calculation software. In this chapter, we have used the calculation software which Risø uses for power quality measurements to calculate the power quality characteristics for both measurements and simulations. This has enabled us to assess the ability of the present simulation model to simulate the power quality characteristics of the wind farm, comparing the measured and simulated power quality characteristics.

IEC 61400-21 specifies power quality characteristics for continuous operation as well as switching operations. In this report, we will only compare the charac-

teristics for continuous operation, based on the same eight 10 minute time series which were used in the previous chapter.

The power quality characteristics specified in IEC 61400-21 for continuous operation are maximum power, reactive power and flicker. Besides, the harmonic characteristics are specified, but they are only required for wind turbines with power converters.

8.2 Maximum power

Both the 200 ms maximum power and the 60 s maximum power have been compared. First, Risøs power quality measurements have been used to compare the measured and simulated maximum powers of wind turbine 1. Then the WINDTEST measurements have been used to compare the maximum of the sum of power from wind turbine 1 and wind turbine 2.

Figure 36 shows the maximum values of the 200 ms average power. The simulated maximum power of the time series with approximately 9 m/s mean wind speed are slightly greater than the measured maximum power. The average difference between simulated and measured maximum is 31 kW or 2 % of the measured maximum, which is a very small difference, taking into account the uncertainty of comparing only six 10 minute time series. Concerning the maximum values of the two time series with approximately 15 m/s mean wind speed the uncertainty is even greater, but the average difference between simulated and measured maximums is –307 kW or 13 % of the measured maximum.

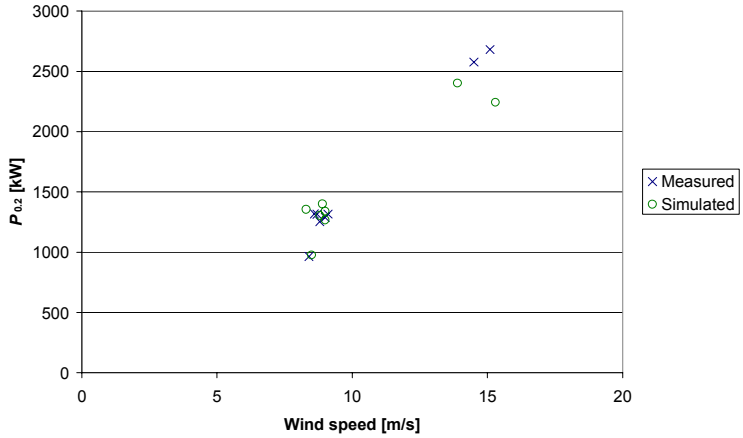

Figure 36. Measured and simulated maximum values of 200 ms average power of wind turbine 1 in the selected eight 10 minute time series.

Figure 37 shows the maximum values of the 60 s average power. The average difference between the maximum values of the simulated and measured power time series with approximately 9 m/s mean wind speed is only 23 kW, whereas the average difference maximum values at approximately 15 m/s mean wind speed is –117 kW, i.e. a closer agreement for with the 200 ms maximum power.

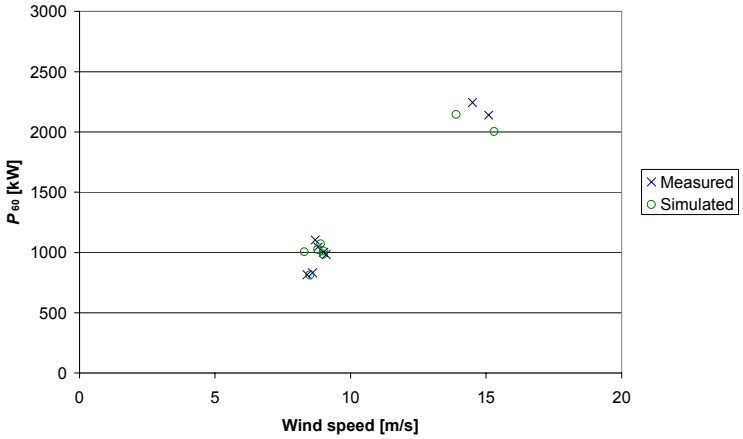

Figure 37. Measured and simulated maximum values of 60 s average power of wind turbine 1 in the selected eight 10 minute time series.

The WINDTEST measurements have been used to compare the maximum values of the sum of power from wind turbine 1 and wind turbine 2. The WINDTEST power measurements are performed with power transducers which have a smaller bandwidth than Risøs power quality measurements. However, comparisons of Risøs and WINDTESTs power measurements on wind turbine 1 have shown that the average difference between the 200 ms maximum power measured with the two systems is only 7 kW, which is neglectable.

Figure 38 shows the maximum values of the 200 ms average power sum. The average difference between the simulated and measured maximum of the sum power of the time series with approximately 9 m/s mean wind speed is 43 kW, i.e. slightly greater simulated than the measured maximum power like for wind turbine 1 alone. The average difference between the simulated and measured maximum values of the two time series with approximately 15 m/s mean wind speed is –385 kW.

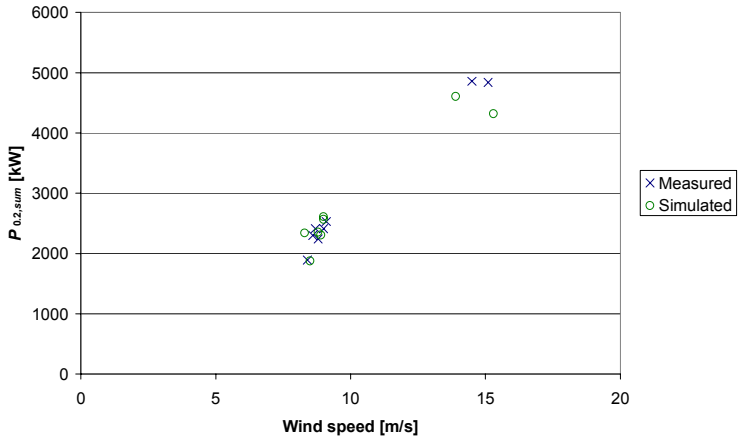

Figure 38. Measured and simulated values of 200 ms average of summed power of wind turbine 1 and wind turbine 2 in the selected eight 10 minute time series.

Figure 39 shows the maximum values of the 60 s average power sum. The average difference between the simulated and measured maximum of the sum power of the time series with approximately 9 m/s mean wind speed is 3 kW, i.e. slightly greater simulated than the measured maximum power like for wind turbine 1 alone. The average difference between the simulated and measured maximum values of the two time series with approximately 15 m/s mean wind speed is –146 kW.

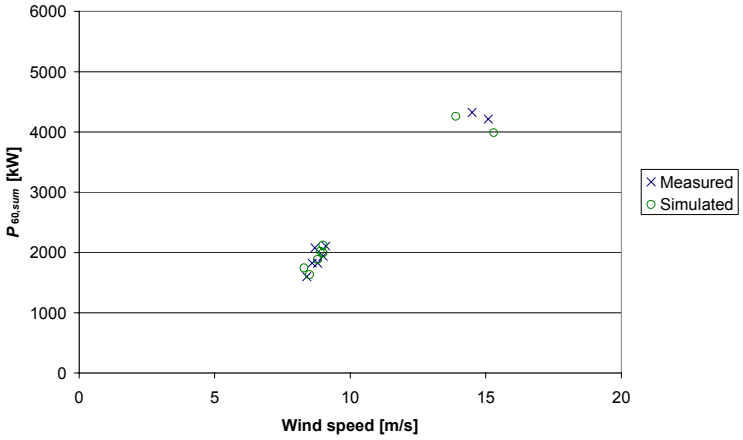

Figure 39. Measured and simulated values of 60 s average of summed power of wind turbine 1 and wind turbine 2 in the selected eight 10 minute time series.

Summarising the above results, the comparisons have shown good agreement between simulated maximum power at approximately 9 m/s, whereas the simulations underestimate the maximum values at 15 m/s, which reflects that the slow fluctuations are not simulated well enough as described in section 7.3. The maximum power stated in the data cheat according to IEC 61400-21 is the maximum of 5 time series for each 1 m/s, i.e. the maximum of approximately 60 time series distributed from 3 m/s to 15 m/s. The present simulation results are very promising, but to be able to make more accurate simulations of the IEC 61400-21 maximum values, an improvement of the simulation in the stall region is desirable. Inclusion of the transversal wind speed components could be necessary to obtain better simulation results.

8.3 Reactive power

The 10 minutes mean values of the reactive power vs. active power of the selected six time series with mean wind speed 9 m/s are shown in Figure 40. We see a very good agreement between the scatter of measured and simulated reactive power for the six runs. The average difference between simulated and measured reactive power is only –6 kvar.

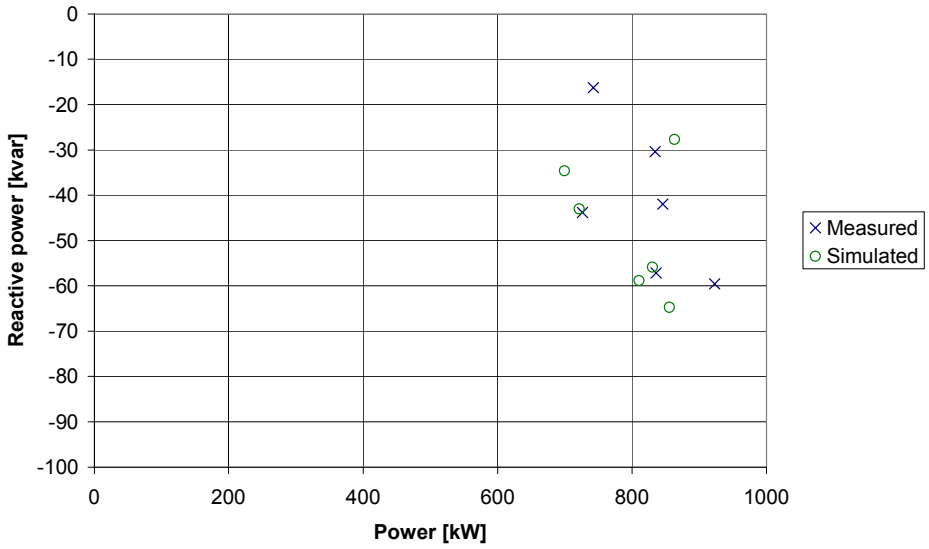

Figure 40. 10 min mean values of reactive power vs. active power.

The reactive power stated in the data sheet according to IEC 61400-21 is the bin averages of the approximately 60 time series, distributing the measurements in 10 % bin of the active power. These values appear to be very well simulated using the six runs at 9 m/s.

8.4 Flicker for continuous operation

In IEC 61400-21, the flicker coefficient c is defined to characterise the flicker emission from a wind turbine during continuous operation. The flicker coefficient is specified for different grid impedance angles ψ_k, and the flicker coefficient $c(\psi_k)$ is according to

$$P_{st} = c(\psi_k) \cdot \frac{S_n}{S_k} \tag{66}$$

where P_{st} is the short term flicker emission from the wind turbine with rated apparent power S_n on a grid with the short circuit power S_k.

The flicker coefficient strongly depends on the grid impedance angle, because active power fluctuations contribute strongest to flicker emission at lower grid impedance angles, while reactive power fluctuations contribute strongest to flicker emission at higher grid impedance angles. For angles in between, the flicker emission from a wind turbine is often smaller than for higher as well as lower angles, because increasing power (increasing voltage) implies decreasing reactive power (decreasing voltage), i.e. $\partial Q/\partial P<0$.

IEC 61400-21 requires the flicker coefficients to be specified for four grid impedance angles: 30 deg, 50 deg, 70 deg and 85 deg. Figure 41, Figure 42, Figure 43 and Figure 44 show the measured and simulated flicker coefficients of the selected eight time series for each of the four grid impedance angles. Again, we see a very good agreement at 9 m/s, while the underestimated fluctuations at 15 m/s causes lower simulated flicker emission than measured flicker emission.

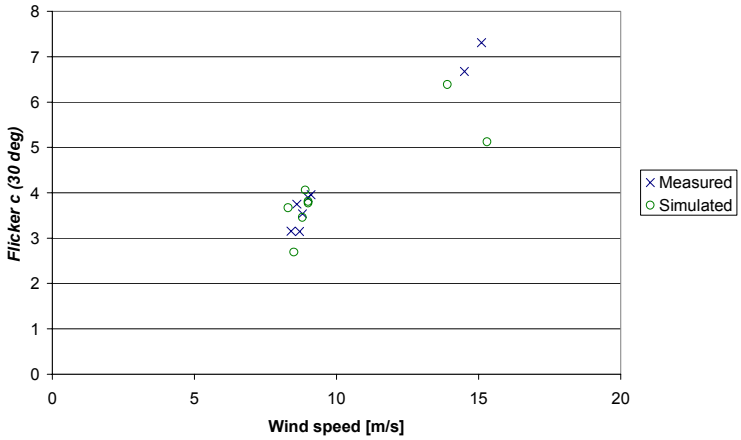

Figure 41. Measured and simulated flicker coefficients for continuous operation of wind turbine 1. Grid impedance angle 30 deg.

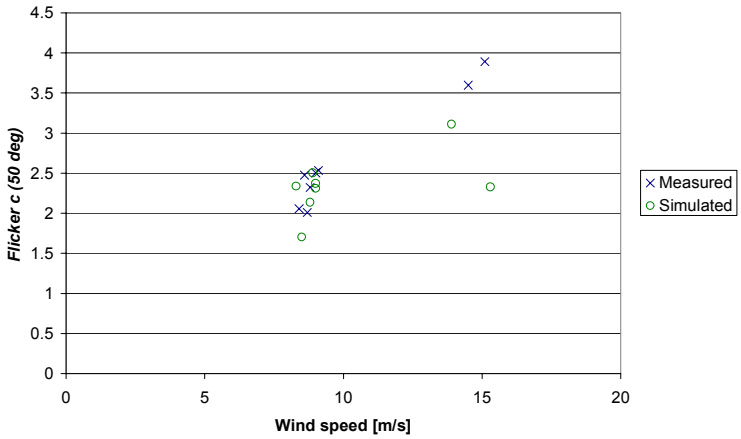

Figure 42. Measured and simulated flicker coefficients for continuous operation of wind turbine 1. Grid impedance angle 50 deg.

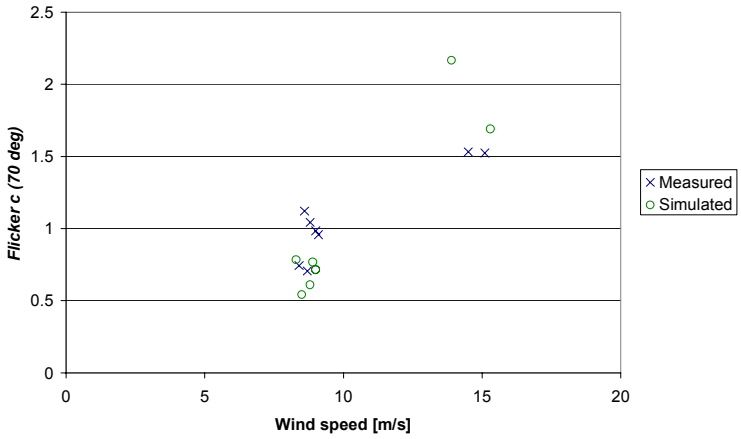

Figure 43. Measured and simulated flicker coefficients for continuous operation of wind turbine 1. Grid impedance angle 70 deg.

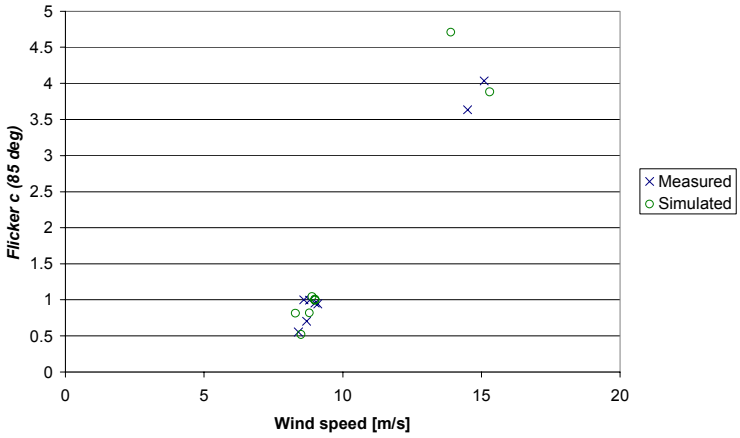

Figure 44. Measured and simulated flicker coefficients for continuous operation of wind turbine 1. Grid impedance angle 85 deg.

For the data sheet, IEC 61400-21 requires the 99th percentile of weighted flicker coefficients, taking into account the wind speed distribution. As the 99th percentile of the flicker coefficients is often determined by the values at high wind speeds, it is essential to predict accurate values at high wind speeds. Inclusion of the transversal wind speed components is likely to improve the simulation results, because it will increase the power fluctuations at higher wind speeds.

9 Conclusion

A dynamic model of the wind farm Hagesholm has been implemented in the dedicated power system simulation program DIgSILENT. The model has been verified using simultaneous power quality measurements on the 10 kV terminals of a single wind turbine and power performance measurements on two wind turbines. The verification shows a generally good agreement between simulations and measurements, although the simulations at higher wind speeds seem to underestimate the power and voltage fluctuations. This can be improved by extending the wind model.

The 10 kV AC power collection system in the wind farm has been modelled together with the substation transformers. The 50 kV grid is represented by a simple Thevenin equivalent. This is an adequate grid model to study the influence of the wind farm on the power quality of the 10 kV grid at stationary conditions.

The electric models of the six wind turbines include tower cables, step-up transformers, capacitor banks, softstarters and induction generators. The mechanical wind turbine model includes the dynamics of the drive train, modelled as a two mass model with wind turbine rotor inertia and generator inertia connected through a flexible, damped shaft.

The wind turbine aerodynamic model includes dynamic stall effects using a C_p based method with three C_p tables, one for steady state, one for unseparated flow and one for separated flow. This corresponds to conventional dynamic stall models, only we interpolate in the C_p tables instead of the aerodynamic lift tables which are normally used.

The wind models include the coherence between the wind speeds at different wind turbines as well as the 3p effects of turbulence and tower shadow wind

speed fields at the individual wind turbine rotor disks. The coherence between the wind turbines is included to account for the summation effects of power from more wind turbines, whereas the 3*p* effect is essential for simulation of the fluctuations which contribute to the flicker emission during continuous operation of the wind farm.

The model has been verified using six 10 minute measurements with mean wind speeds at about 9 m/s and two 10 minute measurements with mean wind speeds at about 15 m/s. The comparisons of power and voltage fluctuations at about 9 m/s show a very good agreement between measurements and simulations up to about 1 Hz. Better results can be obtained above 1 Hz with extensions of the wind model and of mechanical model.

The comparisons of power fluctuations at about 15 m/s show that the simulations underestimate the fluctuations in the stall region. The difference is less than 15 %, but this can probably be improved by including the transversal components of the wind speed in the model.

The model has been used to asses the ability of the simulation models to predict the influence of the wind farm on the power quality characteristics of wind turbines specified in IEC 61400-21. These comparisons have shown that the underestimation of power fluctuations in the stall region influences the prediction of power quality characteristics, whereas the influence of fluctuations above 1 Hz are not so important for the prediction of power quality.

Acknowledgements

The Danish Energy Agency is acknowledged for funding this work in contract 1363/00-0003. A special thanks is given to North-West Sealand Energy Supply Company, NVE, who has participated in the project discussion on own funding and assisted in the power quality measurements. Also thanks to the Danish transmission system operators Eltra and Elkraft System, who have also provided useful experience as members of an advisory committee for the project. Finally thanks to SEAS Wind Energy Centre for funding to maintain the Vindeby data, which has been used in this report.

References

[1] International Wind Energy Development - World Market Update 1999. BTM Consults Aps. Ringkøbing, Denmark March 2000 ISBN 87-987788-0-3

[2] Energy 21. The Danish Government's Action Plan. The Danish Energy Agency, April 1996.

[3] Draft IEC 61400-21. Ed.1: Wind turbine generator systems – Part 21: Measurement and assessment of power quality characteristics of grid connected wind turbines. Committee Draft for Vote (CDV) International Electrotechnical Commission, IEC 2000-06-09.

[4] KR111-E. Connection of Wind Turbines to Low and Medium Voltage Networks. Elteknikkomiteen 1998-10-09.

[5] Tilslutningsbetingelser for vindmølleparker tilsluttet transmissionsnettet. 2. udgave. Eltra April 2000.

[6] Tilslutningsbetingelser for vindmølleparker tilsluttet eltransmissionsnettet. 1. udgave. Elkrafts Netudvalg Juli 1999.
[7] DIgSILENT PowerFactory Manuals Version 12.0. 2001.
[8] DIgSILENT note on asynchronous machine models.
[9] V.Achmatov, H.Knudsen, A.H.Nielsen. Advanced simulation of windmills in the electric power system. Electrical Power and Energy Systems 22, p.421-434. Elsevier 2000.
[10] S.Øye, Dynamic stall - simulated as time lag of separation. 1991. Proceedings of the 4th IEA Symposium on the Aerodynamics of Wind Turbines, McAnulty, K.F. (Ed), Rome, Italy.
[11] L. Kristensen and S. Frandsen. Model for power spectra of the blade of a wind turbine measured from the moving frame of reference. Journal of Wind Engineering and Industrial Aerodynamics, 10 (1982).
[12] J. Tande, P. Sørensen, M. Galal, U. Naoman, E. Mansour, A. Hewehy, A. Maghawry and I. Darweesh: Hurghada Wind Energy Technology Center Demostration Wind Farm Studies. Power Quality Assessment. Risø-I-1141(EN). September 1997.
[13] P.Sørensen. Methods for calculation of the flicker contribution from wind turbines Risø-I-939, 1995. Risø National Laboratory, Roskilde, Denmark.
[14] Jakob Mann. The spectral velocity tensor in moderately complex terrain. Journal of Wind Engineering and Industrial Aerodynamics 88 (2000), pp. 153-169.
[15] N.O.Jensen. A note on wind generator interaction. Risø M 2411. November 1983.
[16] S.Frandsen and M.L.Thøgersen. Integrated fatigue loading for wind turbines in wind farms by combining ambient turbulence and wakes. Wind Engineering vol.23 No.6, pp.327-340.
[17] P.A.C. Rosas, P. Sørensen and H. Bindner. Fast wind modelling for wind turbines. Proceedings for special topic wind energy conference. Kassel 2000.
[18] A.I.Estanqueiro, R.F.Aguiar, J.A.G.Saraiva, R.M.G.Castro and J.M.F.D.Jesus. On the effect of utility grid characteristics on wind park power output fluctuations. Proceedings of British Wind Energy Conference BWEA'15. York 1993.
[19] Shinozuka, M. and C.M.Jan. Digital simulations of random processes and its applications. Journal of sound and vibration, vol.25, No.1, pp.111-128. 1972.
[20] J.Mann. Wind field simulation. Prob. Engng. Mech. Vol. 13 No. 4. Elsevier 1998.
[21] P.Sørensen, B.Bak-Jensen, J.Kristiansen, A.D.Hansen, L. Janosi and J.Bech. Power plant characteristics of wind farms. Wind Power for the 21st Century. Proceedings of the International Conference held at Kassel, Germany 25-27 September 2000.
[22] P.S.Veers. Three-Dimensional Wind Simulations. SAND88-0132. Sandia National Laboratories, Albuquerque, New Mexixo, 1988.
[23] Kaimal,J.C., J.C.Wyngaard, Y.Izumi and O.R.Coté. Spectral characteristics of surface layer turbulence. Q.J.R.Meteorol. Sooc. 1972, 98, pp.563-598.
[24] Dansk Ingeniørforenings og Ingeniør-sammenslutningens norm for last og sikkerhed for vindmøllekonstruktioner. 1. udgave maj 1992. Dansk Standard DS 472.
[25] ENV 1991-2-4. Eurocode 1: Basis of design and actions on structures – Part 2-4: Actions on structures – Wind actions. CEN European Committee for Standardization. Brussels May 1995.

[26] Højstrup,J., S.E.Larsen and P.H.Madsen. Power spectra of horizontal wind components in the neutral atmospheric boundary layer. In Ninth Symposium of Turbulence and Diffusion, ed. N.O.Jensen, L.Kristiansen and S.E.Larsen. American Meteorology Society, 1990, pp.305-308.
[27] Davenport, A.G. The spectrum of horizontal gustiness near the ground in high winds. Quart. J. Roy. Meteorol. Soc. 87, 194-211.
[28] W. Schlez and D. Infield. Horizontal, two point coherence for separations greater than the measurement height. Boundary-Layer Meteorology 87. Kuvwer Academic Publishers, Netherlands 1998.
[29] W.Langreder. Models for Variable Speed Wind Turbines. M.Sc. Thesis, CREST Loughborough University and Risø National Laboratory, 1996.
[30] P.H.Madsen and F.Rasmussen. Rotor loading on a three-bladed wind turbine. European Wind Energy Conference, Glasgow EWEC'89
[31] P.Sørensen, G.C.Larsen and C.J.Christensen. A complex frequency domain model of wind turbine structures. Journal of Solar Energy Engineering. November 1995, Vol.117, pp.311-317.
[32] P.Sørensen. Frequency domain modelling of wind turbine structures. Risø-R749(EN). 1994.
[33] Ekelund, F.A. Hydrodynamik. Newtonske væskers mekanik. (Den private Ingeniørfond). 322 pp. 1968.
[34] IEC 831-1. Shunt power capacitors of the self-healing type for a.c. systems having a rated voltage up to and including 1000 V, General performance, testing and rating – safety requirements – Guide for installation and operation. Second edition 1996-11.

Appendix A. Measurement and simulation results

This appendix shows simulations compared to measurements for 8 runs selected for the verification.

Table 3. Main statistical data measured for the selected 10 minute runs. The corresponding statistical data for the simulations are shown in brackets.

Date and time	Mean wind speed [m/s]	Turbulence intensity [%]	Wind direction [deg]	Power turbine 1 [kW]	Power turbine 2 [kW]
12 Mar 01 18:17	8.6 (8.3)	10.5 (11.8)	237	727 (700)	773 (628)
12 Mar 01 18:31	9.0 (8.9)	10.3 (10.2)	238	834 (831)	833 (837)
12 Mar 01 18:45	9.1 (9.0)	8.7 (8.3)	233	921 (856)	985 (879)
12 Mar 01 18:59	8.7 (8.8)	8.5 (8.7)	229	848 (810)	777 (799)
12 Mar 01 19:13	8.8 (9.0)	9.4 (8.8)	230	835 (864)	770 (897)
12 Mar 01 19:27	8.4 (8.5)	6.2 (6.3)	233	743 (721)	713 (719)
12 Mar 01 10:54	15.3 (15.1)	14.1 (13.7)	218	2020 (1974)	1976 (1972)
12 Mar 01 11:07	14.5 (13.9)	14.9 (15.1)	219	1943 (2009)	2017 (2011)

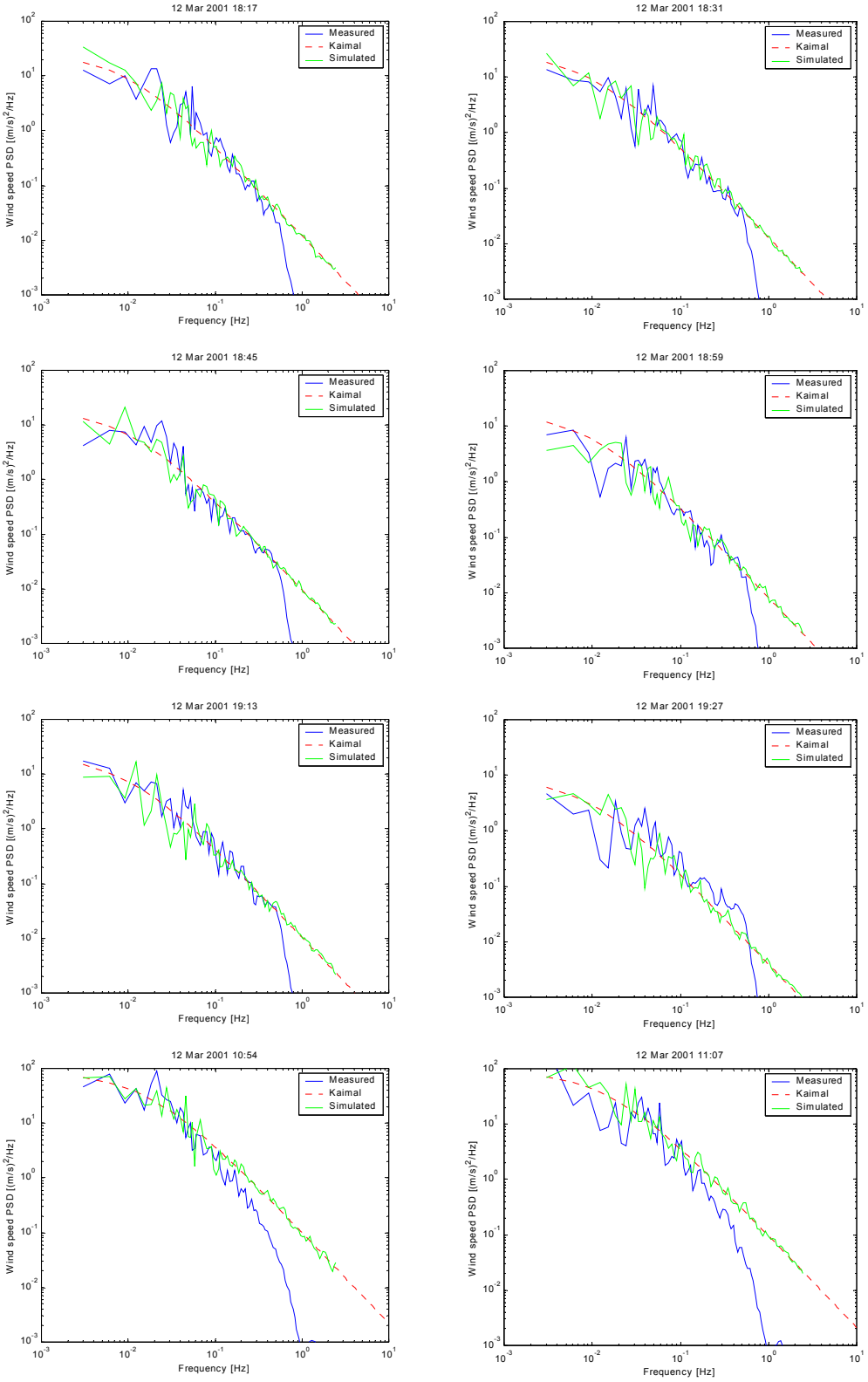

Figure 45. Power spectral densities of measured and simulated wind speeds in hub height. The estimated Kaimal spectrum is also shown.

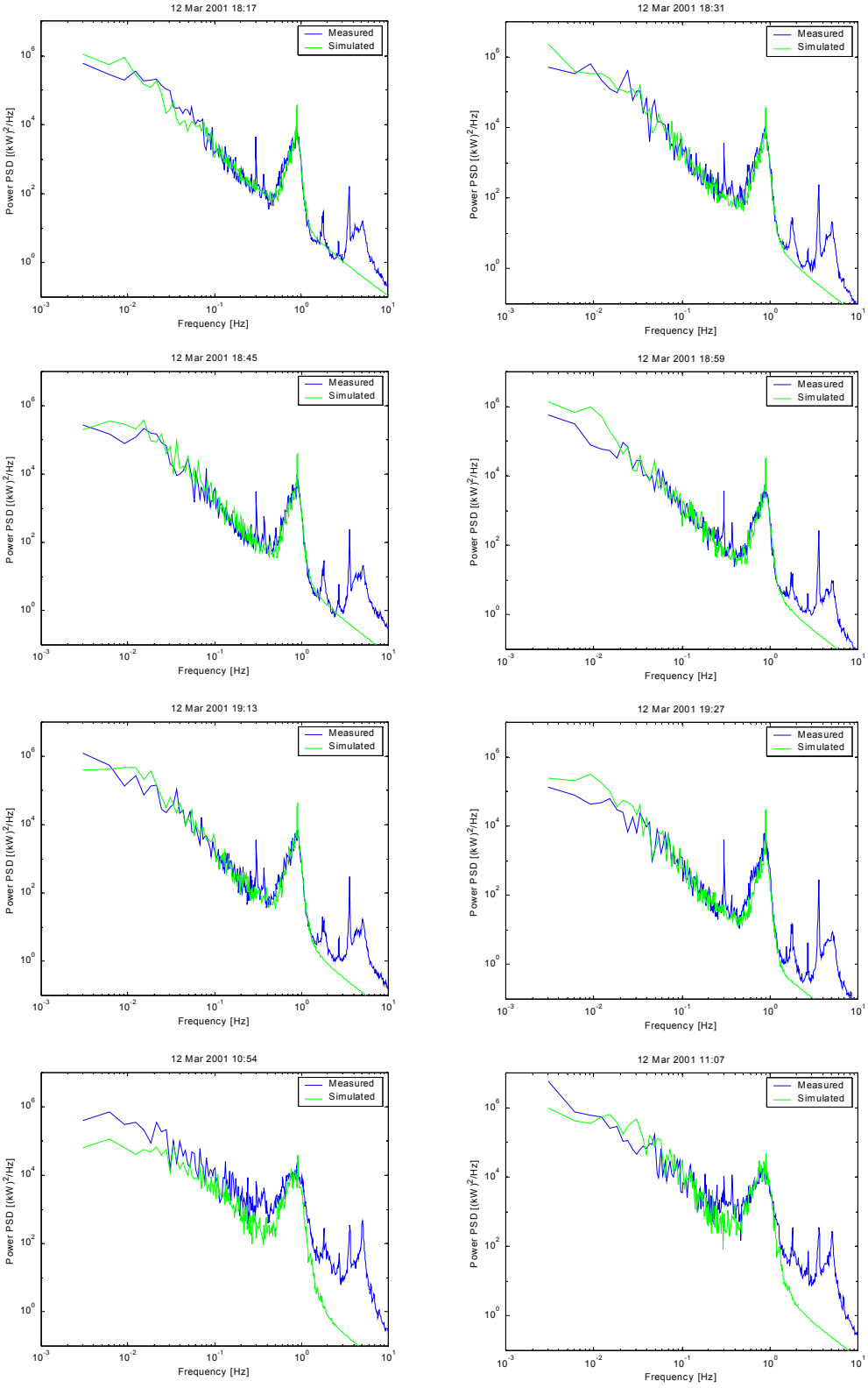

Figure 46 Power spectral densities of measured and simulated active power.

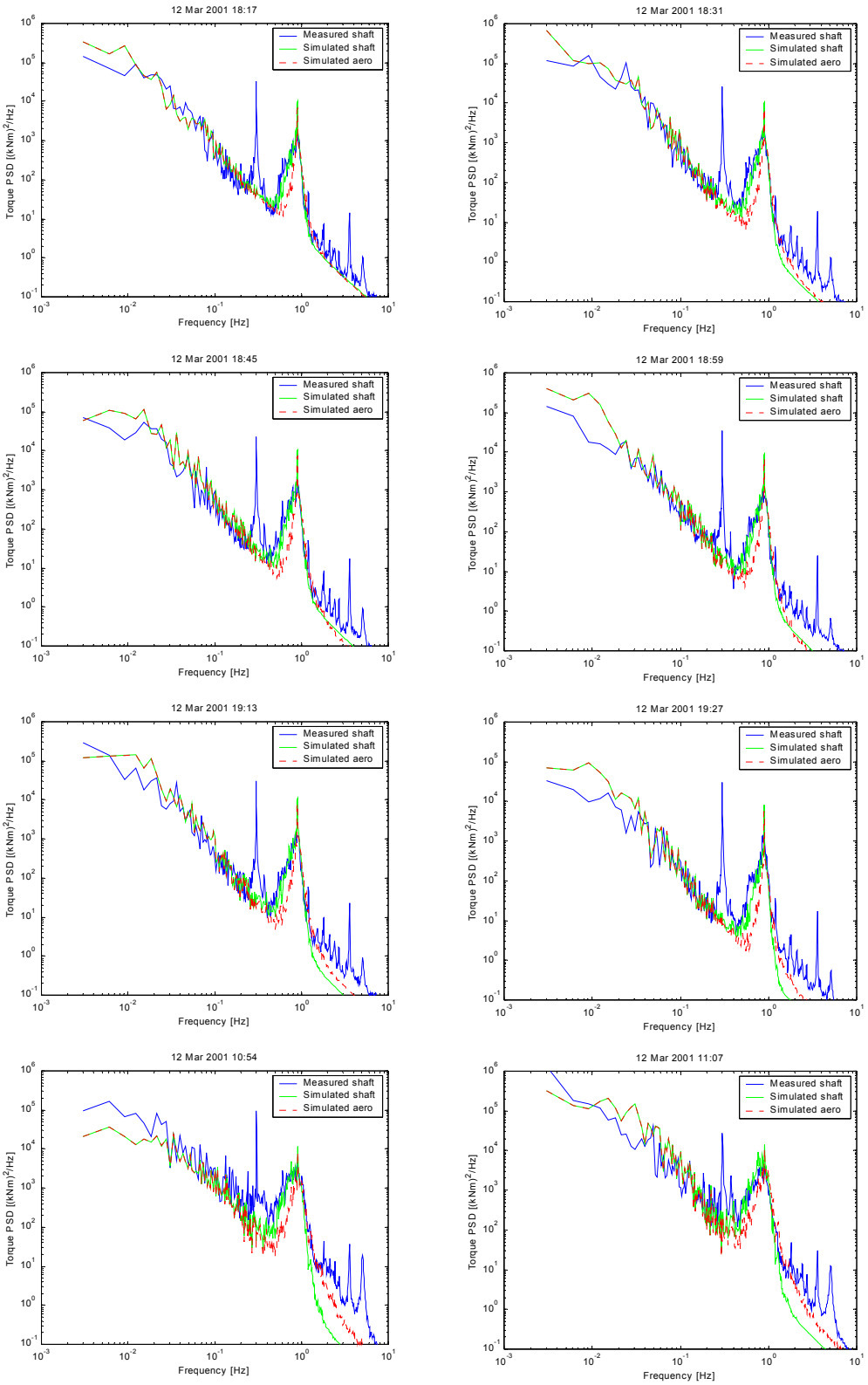

Figure 47 Power spectral densities of measured and simulated torque.

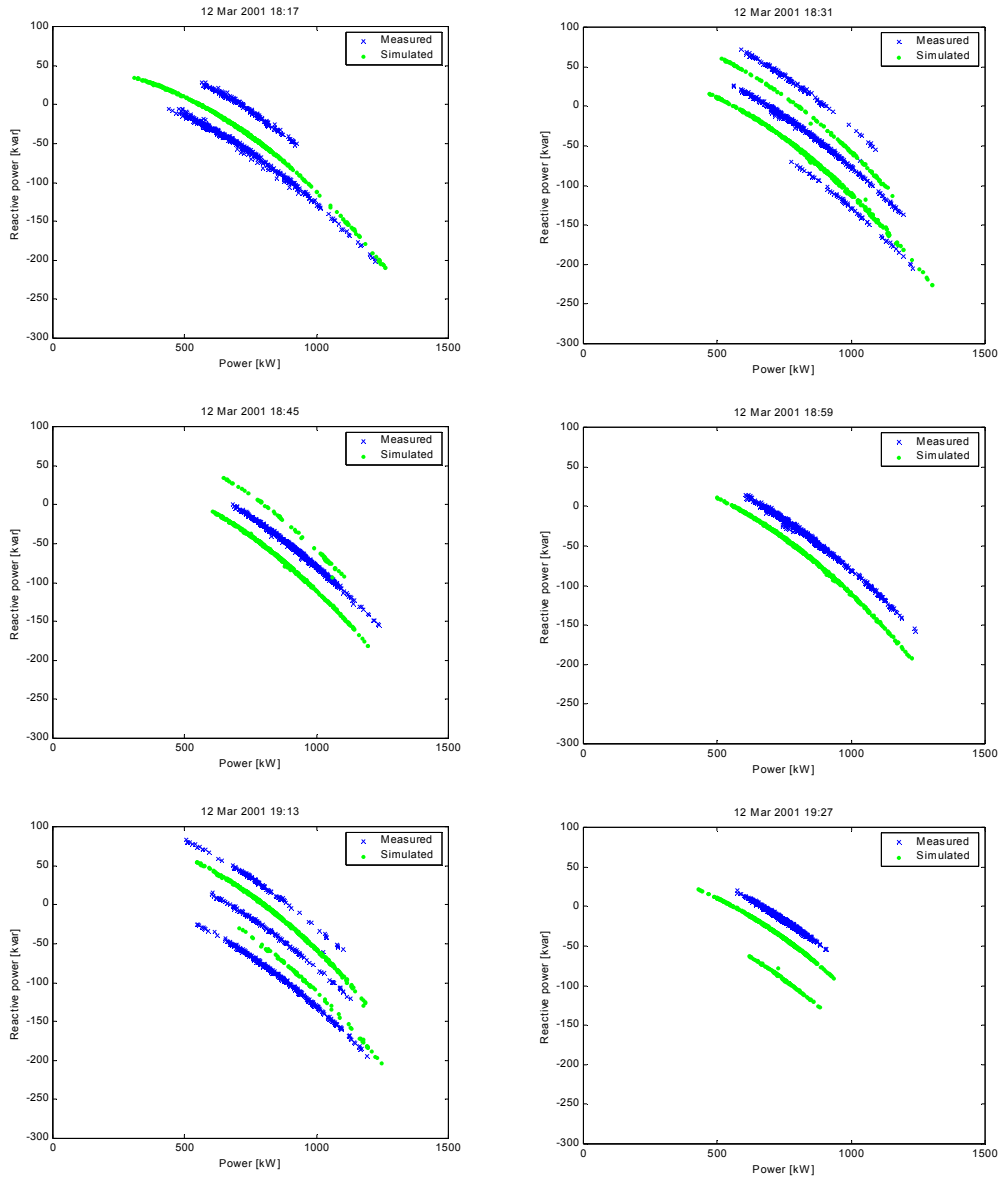

Figure 48. One second average values of measured and simulated reactive power vs. active power.

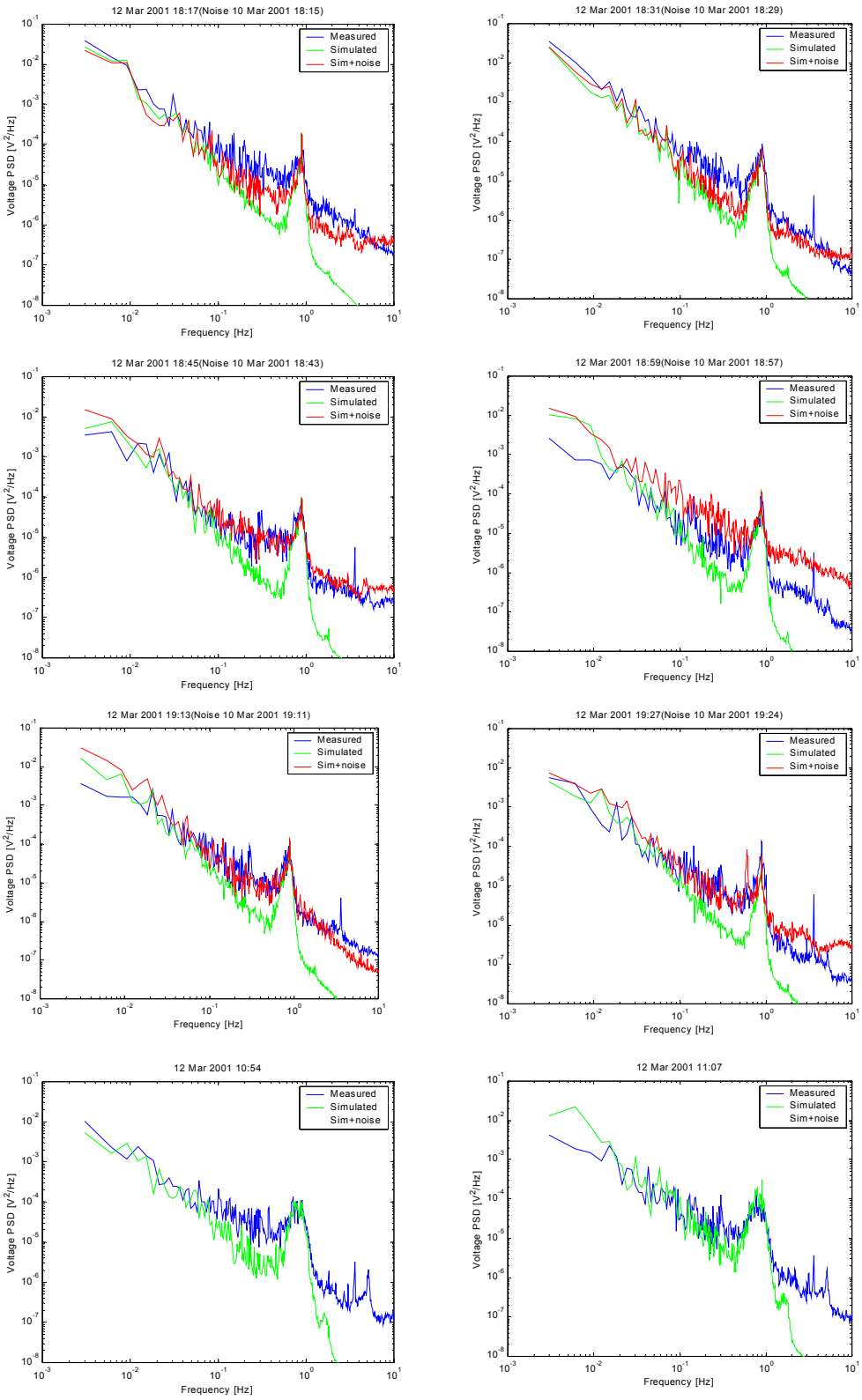

Figure 49. PSDs of measured and simulated voltage. Also PSDs of simulated voltage fluctuations plus measured background fluctuations are shown

Bibliographic Data Sheet **Risø-R-1281(EN)**

Title and authors

Simulation of interaction between wind farm and power system

P.Sørensen, A.D.Hansen, L.Janosi, J.Bech and B.Bak-Jensen

ISBN	ISSN
ISBN 87-550-2912-4; ISBN 87-550-2913-2 (Internet)	0106-2840

Department or group	Date
Wind Energy Department	December 2001

Groups own reg. number(s)	Project/contract No(s)
1115018-00	EFP 1363/00-0003

Pages	Tables	Illustrations	References
65	3	49	34

Abstract (max. 2000 characters)

A dynamic model of the wind farm Hagesholm has been implemented in the dedicated power system simulation program DIgSILENT. The wind farm consists of six 2MW NM2000/72 wind turbines from NEG-Micon. The model has been verified using simultaneous power quality measurements on the 10 kV terminals of a single wind turbine and power performance measurements on two wind turbines. The verification shows a generally good agreement between simulations and measurements, although the simulations at higher wind speeds seem to underestimate the power and voltage fluctuations. A way to improve the simulation at higher wind speeds is suggested.

Descriptors INIS/EDB

COMPUTERIZED SIMULATION; ELECTRIC POTENTIAL; ELECTRIC POWER; FLICKER; FLUCTUATIONS; MATHEMATICAL MODELS; PERFORMANCE; POWER SYSTEMS; VERIFICATION; WIND TURBINE ARRAYS; WIND TURBINES

Available on request from Information Service Department, Risø National Laboratory,
(Afdelingen for Informationsservice, Forskningscenter Risø), P.O.Box 49, DK-4000 Roskilde, Denmark.
Telephone +45 4677 4004, Telefax +45 4677 4013